A physics-based flow stress model for chip formation simulation when machining Alloy 718

Journal of Materials Processing Tech. 352 (2026) 119316

Contents lists available at ScienceDirect

Journal of Materials Processing Tech.

journal homepage: www.elsevier.com/locate/jmatprotec

Research article

A physics-based flow stress model for chip formation simulation when machining Alloy 718

Tobias Cyra-Wolf [a,*], Amir Malakizadi [b,c], Jannis Saelzer [a], Youssef Alammari [d], Dirk Biermann [a]

[a] Institute of Machining Technology, TU Dortmund University, Baroper Str. 303, Dortmund 44227, Germany
[b] Division of Materials and Manufacture, Department of Industrial and Materials Science, Chalmers University of Technology, Göteborg SE-412 96, Sweden
[c] Inspire AG, Technoparkstrasse 1, Zürich 8005, Switzerland
[d] Department of Mechanical Engineering, College of Engineering, Qassim University, Buraydah 51452, Saudi Arabia

ARTICLE INFO

Keywords:
Drilling
Nickel-base alloy
Material characterisation
Flow stress model
Friction model
Finite Element Method

ABSTRACT

In research on machining technology, simulating chip formation is increasingly essential for understanding the interaction between the cutting edge and workpiece in the shear zones. For this purpose, accurate descriptions of material-specific flow behaviour are decisive and in particular phenomenological models commonly used to approximate the strains and stresses involved. However, challenges remain in accounting for the effects of varying microstructure on chip formation and thermomechanical loads. This study introduces a physics-based constitutive model designed to address this limitation. The flow stress model incorporates microstructure characteristics, such as grain size and the size and volume fractions of strengthening precipitates, to enhance the numerical analysis of chip formation and related thermomechanical loads on cutting tools during machining. A comprehensive material characterisation, including metallographic analyses and Split-Hopkinson-Pressure-Bar (SHPB) tests, reveals the alloy's flow behaviour, allowing for the establishment of flow stress models for different material conditions of the difficult-to-machine nickel-based Alloy 718. In comparison with reference simulations using a Johnson–Cook flow stress model to analyse a drilling process, the accuracy of a physics-based constitutive model in 3D simulations is evaluated, showing a deviation in drilling torque of $\Delta M_z = -0.88\%$ compared to experimentally measured process forces. Validation is achieved through experimental data providing mechanical tool loads and in-situ high-speed recordings to assess calculated chip formation.

1. Introduction

Machining of nickel-based alloys, such as Alloy 718, involves high thermomechanical loads acting on the cutting tool with simultaneous impact on surface integrity of safety-critical components used in the fields of aerospace and oil industries, where durability and reliability are of paramount importance [1,2]. To address these requirements, a detailed process analysis is needed to enhance the understanding of material behaviour during chip formation and to identify the fundamentals that define surface quality and tool wear. Xu et al. [3] developed a pendulum-based cutting test to investigate the prevailing mechanisms that affect surface integrity and chip formation during machining of Alloy 718. Their study experimentally characterised microstructure formation under varying cutting speeds and associated energy consumption during tool engagement. In doing so, the influence of cutting conditions on surface integrity was emphasised by identifying that higher cutting speeds result in larger material deformations and increased grain misorientation. Liao et al. [4] analysed the orthogonal cutting of advanced nickel-based alloys, noting machining characteristics related to differing fractions of γ'. Increasing cutting parameters resulted in high cutting temperatures for both of the selected materials, but reduced cutting energy for low γ' variants due to a softening effect. However, a simultaneously deteriorated surface quality characterised by significant surface damage highlights the crucial role of microstructure in the machinability of nickel-based alloys. Liao et al. [5] also focused on Alloy 718, conducting metallurgical investigations on machined surfaces resulting from rough and finish milling of Alloy 718, amongst other manufacturing processes. This post-process analysis of the conventional machining emphasises the formation of white layers and material drag due to thermomechanical loads on the grain structure during chip formation in machining of difficult-to-machine nickel-based alloys. Olovsjö et al. [6] examined how the microstructure influences tool wear, finding

* Corresponding author.
E-mail address: tobias2.wolf@tu-dortmund.de (T. Cyra-Wolf).

https://doi.org/10.1016/j.jmatprotec.2026.119316
Received 8 December 2025; Received in revised form 6 April 2026; Accepted 6 April 2026
Available online 7 April 2026

that large grains cause significant notch wear at the cutting edge during turning of wrought Alloy 718. Compared to small grain materials, notch wear increased by 180% in the presence of large grains. The authors, however, observed that flank wear development depended more on material hardness and abrasive carbides than on grain size. Cedergren et al. [7] further asserted that grain size is more critical for notch wear than feed rate adjustments. Singh et al. [8] reported that heat treatment significantly affects the microstructure of Alloy 718, altering its machinability by influencing grain size and also hardness, which in turn, impacts flank wear evolution. Liu and He [9] investigated tool wear progression when drilling Alloy 718 and reported abrasion by hard carbide particles as the dominant wear mechanism. Furthermore, the low thermal conductivity and high work-hardening are believed to have a major role in accelerated tool degradation, particularly in the investigated drilling operations characterised by a confined contact zone that significantly restricts heat dissipation.

By reflecting these discussed scientific results, it can be stated, that the microstructural condition of Alloy 718 has a substantial influence on its machinability, affecting thermomechanical tool loads and tool life. Therefore, understanding the effects of phase specifications is crucial for optimising machining processes. This is particularly important for late execution of drilling operations in the manufacturing value chain, where analysing cutting conditions is essential to reduce part rejections due to tool failure. Detailed insights into chip formation are required, and incorporating Finite Element Method (FEM)-based simulations of chip formation can enhance process analysis in conjunction with experimental work. Accordingly, Pang and Wang [10] conducted FEM simulations comparing the machining performance of various micro-textures on the rake face of drilling tools, noting improvements in tool wear since the modified surface involves an increased heat transfer area, which facilitates heat dissipation. Attanasio et al. [11] numerically analysed the impact of tool wear on surface integrity during drilling of Alloy 718 under specific cooling conditions, developing a subroutine for ongoing geometric modifications of tool geometries based on wear conditions to predict wear.

To enable reliable solutions for industrial applications, research on chip formation simulation has to focus on enhancing numerical results by more accurately considering the deformation behaviour of workpiece materials in relation to their complex microstructure. Jafarian et al. [12] analysed the recrystallisation process during the orthogonal machining of Alloy 718 and conducted simulations with varying Johnson–Cook flow stress descriptions to identify the most suitable material constitutive equation. This was achieved through a defined subroutine that accounted for microstructural and microhardness changes in machining, using the Zener–Hollomon parameter and the Hall–Petch equation. The employed models were partly derived from literature on SHPB experiments, achieving strain rates up to $\dot{\varepsilon} = 11000\ s^{-1}$ at temperatures up to $T = 800\ °C$. The simulations showed good agreement with experimental work in terms of grain refinement and hardness. Jafarian et al. [13] further developed flow stress modelling by utilising an algorithm-based methodology to identify convenient material constants for the Johnson–Cook model specific to Alloy 718. However, these phenomenological models are hardly capable of capturing the effects of microstructural variations on mechanical properties resulting from specific manufacturing routes, such as forging, casting, or additive manufacturing. These models commonly base on inverse calibration and the resulting parameters reflect only the given experimental boundaries. Therefore, the models exclusively represent workpiece materials with defined microstructural characteristics, necessitating a complete re-evaluation of model parameters for any modifications to prior manufacturing processes or heat treatments. This reliance on extensive experimental efforts to determine model parameters limits the applicability of these models in cutting simulations.

Consequently, recent research is directed towards refining flow behaviour modelling by analysing fundamental microstructural characteristics to directly describe deformation in machining through adaptations to the fundamental flow stress equation. In this context, Wedberg et al. [14] examined a method to extrapolate a material model calibrated through experimental testing to encompass strains and strain rates observed in metal cutting, which are not achievable in conventional material characterisation tests. Notably, incorporating dislocation-drag effects associated with high strain rates improved the models' predictive capability. However, these models remained inadequate in predicting material behaviour during the cutting process, primarily due to the absence of additional softening mechanisms, particularly dynamic recrystallisation. Liu et al. [15] noted that phenomenological models, such as Johnson–Cook, commonly used for analysing plastic deformation of metals, do not account for the dependence of material flow on dislocation and microstructure evolution, leading to a lack of accuracy. This issue can be addressed by integrating fundamental microstructure evolution laws into a constitutive model derived from thermal activation theory. Considering the material's grain size, a practical application was developed that aligns closely with experimental data. Imbrogno et al. [16] developed a physics-based constitutive model based on the experimental examination of deformation mechanisms primarily influencing material deformation in orthogonal cutting of Waspaloy. Metallurgical analysis showed altered grain shapes, slip activity, and partial recrystallisation, which were incorporated into the modelling approach. The application of this model demonstrated accurate predictions of cutting forces across various cutting parameters and material behaviours. Rinaldi et al. [17] introduced a physics-based constitutive model for Alloy 718 that describes flow stress behaviour by accounting for material resistance to plastic strain, Hall–Petch stress, and strain hardening. FE simulations comparing physics-based models to phenomenological ones revealed a significant reduction in numerical error. In summary, promising alternatives to phenomenological Johnson–Cook models are emerging, capable of incorporating the comprehensive effects of microstructure, such as grain size and the size and fractions of strengthening phases. These constitutive models are versatile in adapting to microstructural alterations, enabling reliable predictions of thermomechanical loads in chip formation simulations without the need for extensive re-evaluation of model parameters.

To this end, this study aims to introduce a physics-based flow stress model that partially circumvents the described limitations of common modelling approaches. This model includes key strengthening and recovery mechanisms and utilises CALPHAD (Computer Coupling of Phase Diagrams and Thermochemistry)-based estimations of size and volume fractions of strengthening γ' and γ'' phases. Consequently, it is adaptive to the microstructural variations induced along the process-chain, for example, during forming process and ageing treatments. Calibration of the flow stress formulation relies on high-strain-rate material analysis utilising SHPB testing integrated with an induction heating system for thermal pre-conditioning. Additionally, friction experiments conducted with a specialised tribometer under machining-like conditions provide a realistic representation of tribological behaviour in the chip formation zone. Subsequently, a preliminary comparative analysis benchmarks the physics-based formulation against the Johnson–Cook constitutive equation within a 2D orthogonal cutting framework. Upon establishing baseline performance, the models are transposed into a full 3D drilling simulation environment, where predictive accuracy is validated against experimental data under realistic operational kinematics. The analysis covers drilling torque, chip formation, and the impact of varying microstructures on mechanical loads. Finally, the prediction accuracy of the physics-based constitutive models is benchmarked against a baseline Johnson–Cook model.

2. Experimental materials and characterisation

This study on physics-based constitutive models begins with a description of the material characterisation methodology, followed by an overview of the simulation design and a presentation of the

experimental validation procedure for the flow stress models.

2.1. Experimental foundation of developing a physics-based constitutive model

The material characterisation of Alloy 718 is initiated by an analysis of the microstructure, focusing on grain size and hardness of samples extracted from different shafts manufactured through distinct routes, including forging and hot rolling prior to conducted heat treatment. The results, depicted in Fig. 1, reveal clear distinctions in the microstructure, allowing for classification into three material conditions (MC1–MC3).

Although the specimens related to MC1 and MC2 are extracted from the same manufacturer's batch, the metallographic analyses reveal substantial deviations regarding grain size and hardness as separate shafts of $d_w = 200$ mm each were used. The average grain size for MC1 is $d = 33$ µm, whereas for MC2, $d = 15$ µm. This 55% difference in mean grain size results in a 6.5% increase in hardness ($H_{MC1} = 446$ HV10 for MC1, $H_{MC2} = 478$ HV10 for MC2) owing to the higher proportion of grain boundaries. MC3 demonstrates a deviation from this pattern, with $d = 9$ µm and hardness $H_{MC3} = 454$ HV10. This material, with a diameter $d_w = 16$ mm, is processed through an alternative manufacturing process, which involves hot rolling instead of forging. Because of this alternative route, factors apart from the average grain size dominate the strength properties, resulting in approximately the same hardness as with the largest grain size in MC1. In addition to the metallographic analysis of the material's microstructure, the executed heat treatment has to be included in the preparation of physics-based flow stress models. In agreement with AMS 5663, for all the material conditions of Alloy 718, the procedure consisted of solution annealing followed by a subsequent precipitation heat treatment. First, the material is heated to a temperature of $T_{sa} = 980$ °C, which has to be maintained for a duration of $t_{sa} = 90$ min before the solution annealing is completed by cooling in water. Subsequently, the precipitation heat treatment is initiated by reaching a temperature of $T_{pht,1} = 720$ °C, which is maintained for $t_{pht,1} = 480$ min. Afterwards, the material has to be cooled at a constant rate of 56 °C/h to a temperature of $T_{pht,2} = 620$ °C, which is to be maintained for the period of $t_{pht,2} = 480$ min.

The averaged chemical composition of the identified material conditions is also in compliance with AMS5663, as presented in Table 1.

Fig. 2 shows SEM (Scanning Electron Microscopy) micrographs of the microstructures corresponding to MC1 and MC3, respectively. The high-resolution images were acquired using a *Tescan Mira 3* microscope to further emphasise the previously identified differences in average grain size, determined as $d = 33$ µm and $d = 9$ µm. As expected, the fine-grained condition exhibits a higher grain boundary area, and grain boundaries can clearly be recognised in Fig. 2a and b. The contrast variation primarily arises from atomic number differences in back-scattered electron imaging, allowing clear differentiation between matrix and Nb-rich secondary phases. EDS (Energy-Dispersive X-ray Spectroscopy) spectra 1,2,5 and 6 acquired from these particles reveal pronounced Nb peaks accompanied by minor Ti contributions, conforming their identification as NbC-type carbides (Fig. 2e,f,i and j). These carbides are predominantly located along grain boundaries, further supporting the determination of particular grain size in the micrographs.

In addition to the described NbC carbides, a high density of needle-shape precipitates is observed, preferentially situated at the grain boundaries as well, but also partially within the grains. Again, EDS analyses of these features are performed and the spectra 3,4,7 and 8 (Fig. 2g, h, k and l) show enrichment in Ni and Nb relative to the γ matrix. The corresponding chemical signature is consistent with the δ (Ni_3 Nb) phase.

The highlighted diversity in microstructure raises the central research question of whether, despite having similar hardness, the microstructure — specifically the averaged grain size — affects the machinability of Alloy 718 and how this impact can be integrated into numerical chip formation simulations using physics-based flow stress models. Therefore, detailed 3D FEM chip formation simulations of drilling are required to assess the performance of the developed constitutive models and to evaluate the prediction of machining characteristics in comparison with experimental data. Before this, the deformation behaviour of the specified material conditions has to be characterised experimentally and converted into the specific flow stress models for incorporation into the boundary conditions of an initial 2D chip formation simulation. In this context, the Split-Hopkinson-Pressure-Bar-Test, described in Fig. 3, is a well-established experimental setup for obtaining data to approximate realistic flow behaviour in chip formation simulations [18,19]. By conducting unidimensional compression tests with varying specimen temperatures — using induction heating monitored by a pyrometer — and varying strain rates, the

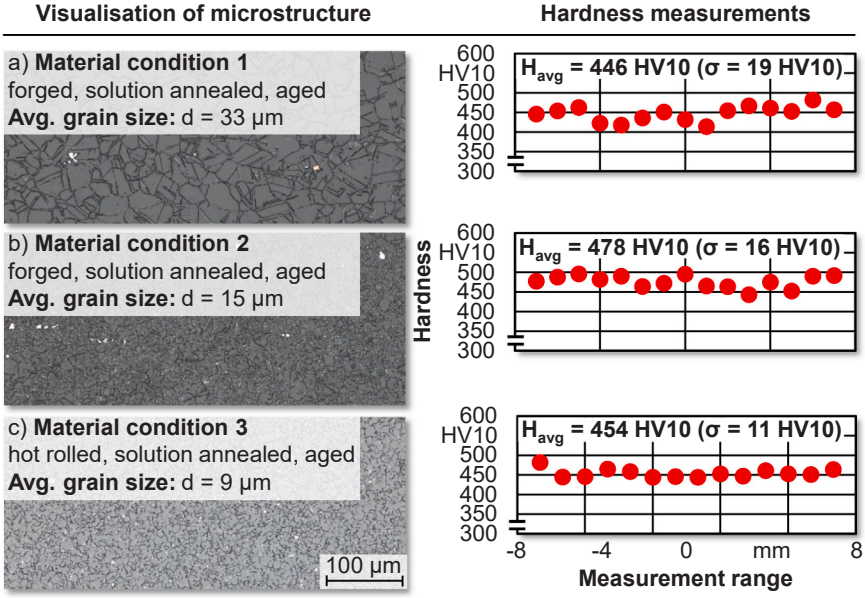

Fig. 1. Comparison of microstructure and hardness of the identified material conditions a) – c). The mentioned standard deviation in Hardness measurements results from the mean value.

Table 1
Chemical composition of the batches of Alloy 718 investigated in this study.

Element	C	Si	Mn	P	S	Cr	Ni	Mo
%	0.03 ± 0.00	0.07 ± 0.02	0.05 ± 0.02	0.008 ± 0.001	0.001 ± < 0.001	18.50 ± 0.02	52.76 ± 0.13	3.06 ± 0.01
Element	Al	Ti	Co	Cu	Nb	Ta	Fe	B
%	0.60 ± 0.01	0.97 ± 0.01	0.13 ± 0.04	0.04 ± 0.01	5.34 ± 0.02	0.01 ± < 0.01	18.41 ± 0.03	0.004 ± < 0.001

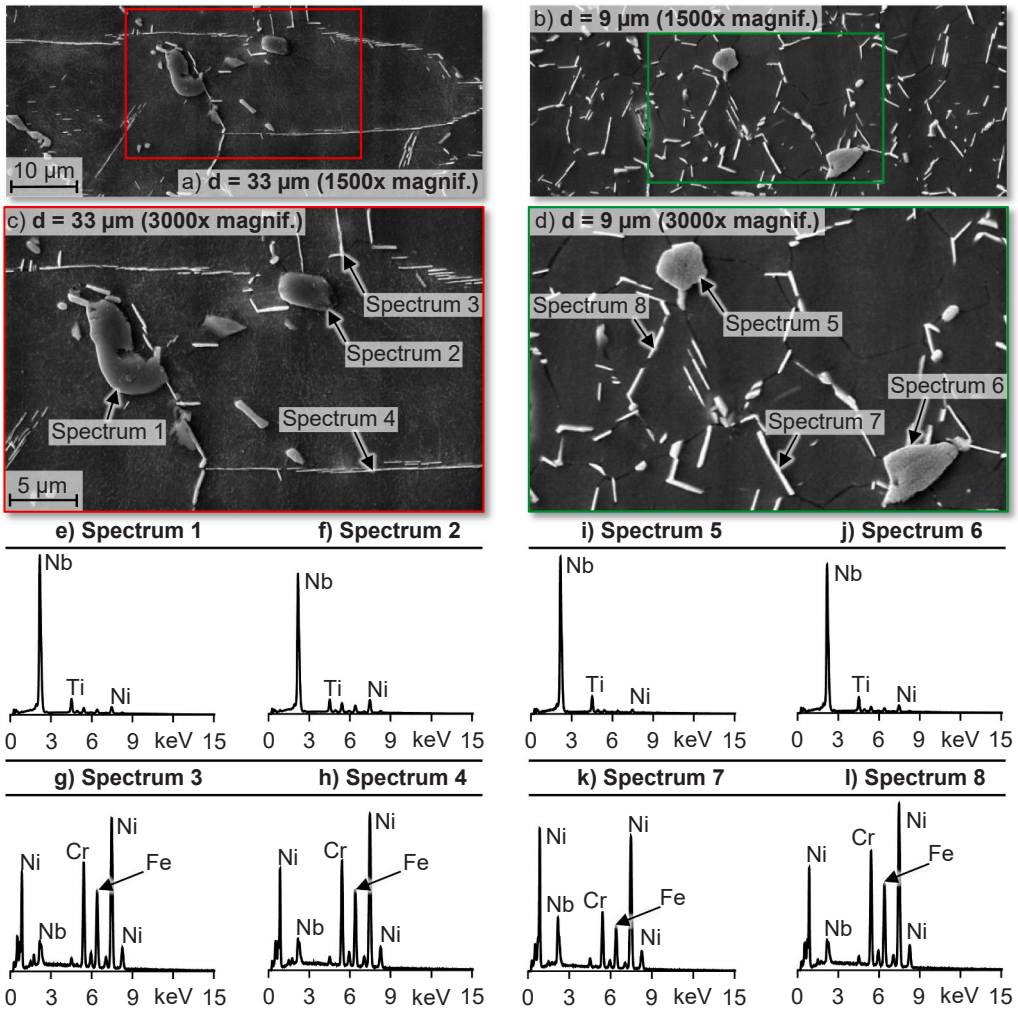

Fig. 2. SEM images revealing the particular microstructures corresponding to the identified material conditions characterised by an average grain size d = 33 µm (a, c, e-h) and d = 9 µm (b, d, i-l).

demanded characterisation of plastic deformation behaviour of the targeted nickel-based alloy can be achieved. From a rough heat conduction calculation based on Fourier's law and preliminary experiments to characterise the emission behaviour of the material samples, in which the temperature was measured on the outer surface and inside the sample, it was determined that the heating system used can produce a homogeneous temperature distribution in the sample within approximately one second. To ensure that this homogeneous temperature distribution is guaranteed in all SHPB tests, the set temperature was maintained for at least three seconds in each case.

The SHPB consists of two aligned bars — the incident bar and the transmission bar — both made of X37CrMoV5. The specimen is positioned centrally between the opposing ends of the bars. Concentrically, an adapted pneumatic pulse generator, connected to an internally guided projectile, is positioned in front of the incident bar. Upon initiation of the experiment, air discharge accelerates the projectile onto the incident bar, generating a compression wave that travels through both components. With a $l_b/d_b > 100$ ratio, a one-dimensional wave propagation is ensured, which is crucial for accurately characterising unidimensional deformation. To prevent plastic deformation of the bars and unintended impact on the specimen, each bar is fitted with a ceramic sheet at the contact area during testing of the high-strength material. However, it has to be noted that the transmission of elastic waves is affected by the inserted sheets, as the ceramic material has a different mechanical impedance. Consequently, the dimensions of these sheets were selected properly to harmonise with the mechanical impedance of the bars. Thus, an influence on the wave propagation is prevented. Strain gauges attached to the bars record the compression wave signal and its progression through the bars and specimen, allowing for calculations of stresses, strains, and strain rates. The theoretical background is detailed in the appendix.

The specimens used in SHPB tests were obtained from workpieces having the introduced material conditions. Experiments were conducted with varying parameter combinations of temperature, $T = 20 \ldots 750\,^{\circ}\mathrm{C}$,

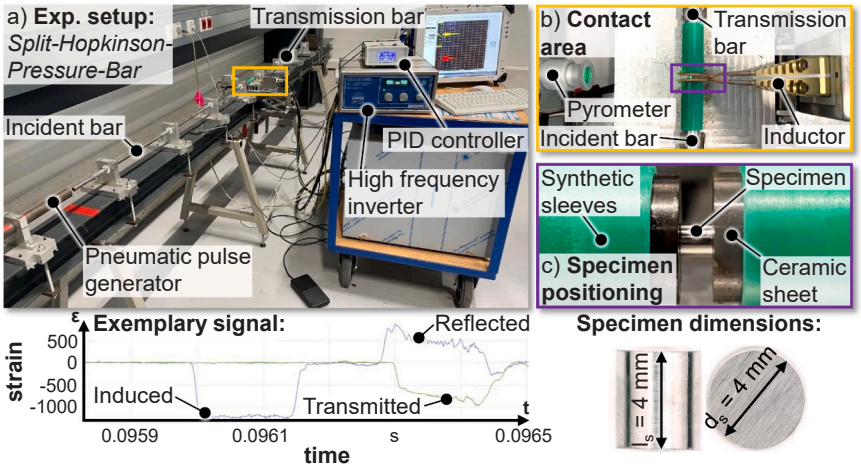

Fig. 3. The experimental setup for SHPB material characterisation (a) with detailed insights into the contact area and the additional equipment (b) as well as the specimen positioning between the incident and the transmission bar, respectively (c).

and impact pressure, $p_L = 1.5 \ldots 2.5$ bar.

2.2. Modelling of preliminary 2D simulations

The deployment of the derived material models requires precursor numerical analysis to benchmark their performance. Consequently, simplified cutting scenarios are simulated first to verify the constitutive response, validating the physics-based model's fidelity before proceeding to full-scale 3D drilling simulations.

Simulations representing orthogonal cutting were executed in DEFORM 13.1, a simulation software developed by Scientific Forming Technologies Corporation. A Johnson–Cook model acquired from Malakizadi et al. [20] serves as a reference and describes the flow stress of Alloy 718 subjected to the standard double-ageing treatment, giving a grain size of $d = 16$ µm and Vickers hardness of $H = 445$ HV10. The chosen material parameters are given in Table 2 and the setup of the 2D simulations is presented in Fig. 4. The FE simulations utilise an incremental Lagrangian formulation. The cutting tool is modelled as a thermally-coupled rigid body, which assumes mechanical rigidity while permitting interfacial heat transfer during chip formation. Material behaviour is defined through tabulated flow stress data generated in MATLAB from the reference Johnson-Cook and physics-based models. The input deck covers strains up to 5, rates up to 10^5 s^{-1} and temperatures up to 1200°C, utilising DEFORM software's logarithmic interpolation scheme to manage the high-strain-rate dependency. The workpiece is set to be elasto-viscoplastic with a minimal element size of $s_w = 0.002$ mm. The workpiece is driven via velocity boundary conditions applied to its bottom edge. A prescribed horizontal velocity generates the relative cutting motion, while the transverse velocity is fully restricted. In accordance with the experimental data available in [20] the simulations were performed with a cutting speed of $v_c = 30$ m/min and $v_c = 60$ m/min. The local mesh refinement is enforced by dynamic mesh windows coupled to the cutting tool that is constrained in both horizontal and transverse direction. This strategy ensures consistent resolution of the shear zones throughout the chip formation process. The cutting tool's mesh is also determined by mesh windows with a minimum element size of $s_t = 0.005$ mm. Since no chip segmentation has been observed in the experimental investigations reported by Malakizadi et al. [20], no damage model is defined in this study. Chip formation is simulated through automatic adaptive remeshing – an in-built functionality in DEFORM. This algorithm manages the severe mesh distortion at the tool tip by periodically regenerating the element topology, thereby facilitating material flow and separation around the cutting edge while preserving numerical stability. Here, adaptive remeshing is triggered by an interference depth of 0.0035 mm.

The thermal properties defined for Alloy 718 in both the Johnson–Cook and the physics-based flow stress models are presented in Fig. 5. The heat transfer in the contact region is modelled with an *HTC* = 100000 kW/m^{2}K which is acquired from [12] and [13] where this value is obtained from FE calibration for the chip formation simulation of similar tool-workpiece combinations.

The complex frictional mechanisms at the tool–chip interface are approximated by a Coulomb-type sliding formulation, in which the apparent friction coefficient μ implemented in the simulations is identified experimentally according to the methodology described in Section 2.4. However, to benchmark its effectiveness, its performance was assessed in comparison with the pressure dependent shear friction model used by Malakizadi et al. [20].

Table 2
Johnson–Cook parameters for aged Alloy 718 [20].

A (MPa)	B (MPa)	C (-)	n (-)	m (-)	$\dot{\varepsilon}_0$ (s^{-1})	T_m (°C)
1562	300	0.0164	0.25	1.7	1	1200

2.3. Modelling the three-dimensional chip formation in drilling process

To conduct the substantial 3D numerical work, the drilling process was modelled in DEFORM 13.1, (see Fig. 6). This is a thermomechanical solid-state simulation in which the influence of the cutting fluid used in the experiments is not represented. The reason for this is that the focus is on the immediate chip formation zone, where the influence of the cutting fluid during drilling is limited. This applies in particular to the mechanical tool loads and chip morphology, which were considered and validated in this study as key simulation results. At industrially relevant cutting speeds, the thermal and mechanical loads are so high that only a negligible portion of the contact areas allow penetration of the cutting fluid. Thus, the cutting fluid cannot have any immediate cooling and lubricating effect in the areas under the highest stress. The CAD models of bore hole bottom and bore hole wall were designed based on the model of the twist drill provided by the cutting tool's manufacturer. The components were positioned and meshed, with particular attention to mesh refinement at the tool's cutting edges in the region of interest. The tetrahedral mesh of the workpiece was provided with a global remeshing method that was initiating the remeshing process for a relative interference depth of 0.7. Just as in the 2D simulations, no damage model is used.

For the simulations, the presented setup utilises the specific flow stress models. It can be adapted with a qualified friction definition selected through specific experimental work, which is described in the

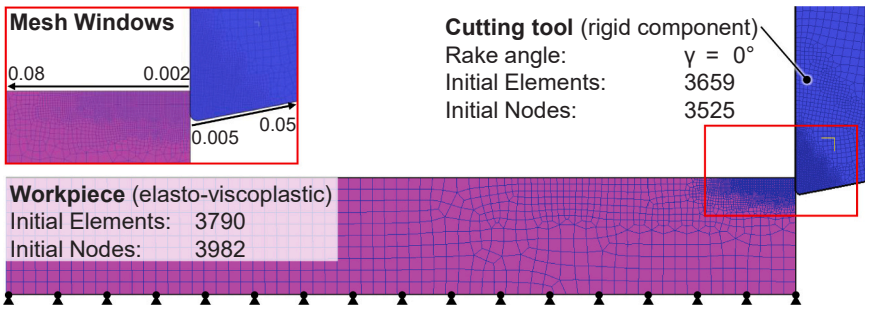

Fig. 4. Boundary conditions of conducted 2D simulations including the meshing strategies of workpiece and cutting tool.

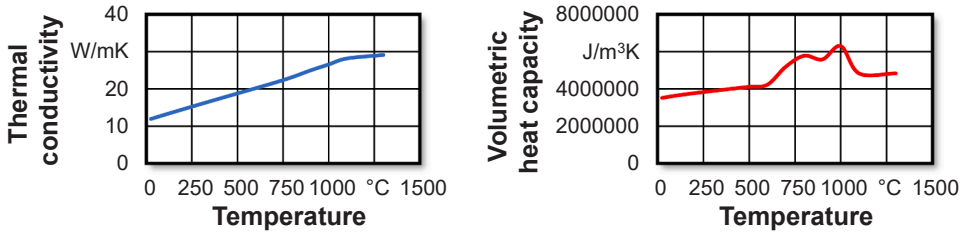

Fig. 5. Thermal properties of Alloy 718 defined in the developed flow stress models.

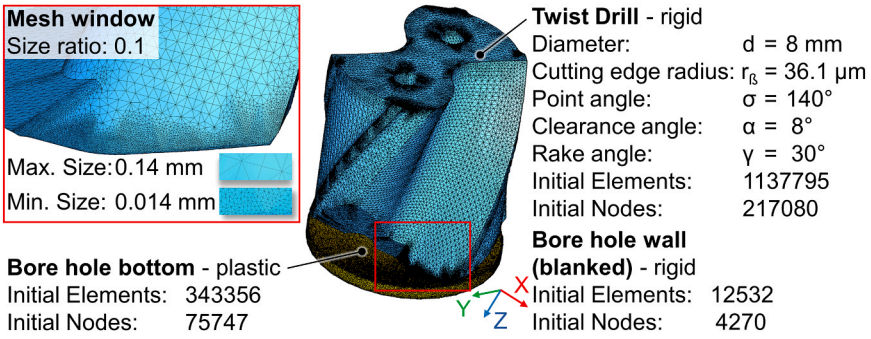

Fig. 6. Boundary conditions of the 3D chip formation simulation including the particularly meshing strategies of the components in contact.

following Section 2.4 and is equipped with the thermal boundaries that were already defined for the 2D simulations. Numerous friction models have been proposed in the literature to address the complex tribological conditions at the tool-chip interface; however, the Coulomb friction model with a constant friction parameter is deemed appropriate. This is because this paper aims to provide an easy-to-recalibrate modelling approach and the calibration of more complex friction models requires a considerable amount of experimentation in order to identify, for example, the shear stress for the Zorev approach or the dependence on temperature or contact normal stress for other model approaches. In addition, previous studies show that simple Coulomb formulations can be used to make predictions of chip formation that are similar in quality to those made using complex approaches [21]. This choice is consistent with previous attempts in literature and effectively satisfies the range of cutting conditions relevant to the drilling process [22].

In accordance with the experimental work, the twist drill, defined as a rigid body, was modelled as a solid carbide tool featuring a two-layer coating approximating the manufacturer's TiN/TiAlN-multilayer specification. The coating exhibits a total thickness of $h_{TiN/TiAlN} = 6$ µm comprising a TiN base layer ($h_{TiN} = 2.4$ µm) and a TiAlN surface layer ($h_{TiAlN} = 3.6$ µm). The distinct thermal properties were obtained from the DEFORM material library, assuming a constant thermal conductivity of $\lambda_{TiN} = 25$ W/mK and a constant volumetric heat capacity of $c_{v,TiN} = 12$ MJ/m^{3}K for the TiN base layer. In contrast, the TiAlN surface layer is described with a temperature dependent thermal conductivity developing from $\lambda_{TiAN,20°C} = 12$ W/mK to $\lambda_{TiAN,1000°C} = 20$ W/mK. The volumetric heat capacity is again defined to be constant with $c_{v,TiAlN} = 15$ MJ/m^{3}K. The kinematics of the drilling process are divided into two consecutive stages, where the cutting tool is initially pushed axially into the bottom, having a predefined wedge shape, with a constant uncut chip thickness of $h = 0.05$ mm throughout the subsequent rotational movement. With this approach, the chisel edge is fully engaged during the simulation, ensuring that realistic interaction between the tool and the workpiece is reproduced. Because of the examined feed $f = 0.1$ mm, this is limited to half a tool rotation to ensure reasonable data availability with a constant uncut chip thickness.

In addition to the physics-based flow stress models, a baseline Johnson–Cook model [20] serves as a benchmark. Similar to the 2D case, the flow stress properties are provided as tabulated data.

The simulations are performed using a Lagrangian incremental method with a cutting tool defined as a rigid body, allowing heat transfer during chip formation. The workpiece is set to be plastic.

2.4. Experimental friction characterisation under cutting-like conditions

The utilisation and subsequent evaluation of the flow stress models derived from the experimental material characterisation during the further procedure require the determination of an adequate friction

model related to the conditions in the chip formation zone. Therefore, an experimental setup is used to determine the behaviour in the secondary shear zones. These conditions are recreated in the special machine tool, *Berger PFS 5558–1*, designed for orthogonal cutting and manufactured by *Heinz Berger Maschinenfabrik GmbH*. The kinematics of the relative motion is here recreated by a main body and a counter body brought into contact owing to a uniaxial movement of the machine table with a relative velocity v_{rel}. Simultaneously, an adjusted dynamometer measures the forces on the clamped main body in two directions (x- and y-directions). The experimental setup was prepared according to Puls et al. [23] to achieve sliding friction with partly Coulomb contact conditions comparable to those in the chip formation zone. The findings of Puls et al. covered apparent friction coefficients resulting from a wide range of relative speeds (v_{rel} = 20 … 100 m/min); however, it is not to be expected that the average relative speed in the secondary shear zones of a drilling process with a cutting speed v_c = 25 m/min is represented.

Thus, the introduced experimental setup is used to determine the process-specific friction behaviour. For this purpose, the friction surface of the main body is oriented with an angle of inclination $\lambda_r = 5°$ to the surface of the counter body, which defines the contact direction and allows the transformation of the measured forces. The fact that the interface between the main body and the counter body is flat, when the angle is taken into account, contributes to the fact that conditions in the contact area are easily adjustable and comparatively evenly distributed, particularly with regard to relative speed, which simplifies transfer to the chip formation zone. The developed experimental setup is illustrated in Fig. 7.

The accuracy of the determined friction characterisation is dependent on the surface topography of the friction pairing [24]. Therefore, the coating deposited on the twist drill used for the machining of Alloy 718 is analysed before the experiments. The examined TiN/TiAlN coating is applied to the wet-blasted substrate using the arc PVD process. Subsequently, the coating procedure is completed by wet surface smoothing. The determination of surface roughness, the elements forming the coating, and the measurement of the cutting edge radius allow the development of specific tools with a defined friction surface serving as the main body in the experiments. In conclusion, the manufactured component was verified regarding its surface topography and subsequently clamped into the dynamometer. Because, under the extreme conditions of continuous drilling, it cannot be assumed that cutting fluid can penetrate the contact surfaces on the tool to any significant extent, the friction model is calibrated for dry conditions and, accordingly, no cutting fluid is added to the friction tests. The counter body intended to execute the relative motion is made of Alloy 718, with an average hardness of H_{avg} = 473 HV10 and an average grain size of d = 25 µm. Therefore, the material is in good agreement with the previously observed material conditions, which is consistent with the original heat treatment. The workpiece is prepared to have a width of w_{cb} = 1 mm and a length of l_{cb} = 140 mm. During the preparation, the counter body was equipped with a chamfer corresponding to $\lambda_r = 5°$ to facilitate the entry into the friction contact.

2.5. Validating the developed physics-based constitutive models

The data intended for validating the 3D simulations is obtained from direct insights into the drilling process, allowing a two-step comparison of simulation and experiment. Alloy 718 is machined with a cutting speed of v_c = 25 m/min and a feed of f = 0.1 mm, which is equivalent to an uncut chip thickness of h = 0.05 mm for each cutting edge. Initially, the drilling torque is measured during a conventional drilling process using a twist drill in its unworn condition, accompanied by a connected rotational dynamometer, *KISTLER 9170 A*. Consequently, an averaged drilling torque can be obtained from five defined measuring intervals of half a tool rotation after reaching the steady state, each of which equals the simulation time t_s = 0.03 s. Additionally, the resulting chips are metallographically prepared for measuring chip thickness, which has to be compared to the chip thickness in the simulations.

The experimental setup, as well as detailed information about the tool and the resulting torque measurements, is shown in Fig. 8.

Furthermore, the actual chip formation during the drilling process can be evaluated using high-speed recordings. For this purpose, a high-speed camera is positioned orthogonally to a rotating acrylic glass tube, which is clamped in the machine spindle. This unit consists of a transparent drilling channel with embedded workpiece material. On the opposite side, a twist drill is fixed in a tool holder equipped with integrated coolant supply. To initiate chip formation, the twist drill is inserted into the transparent drilling channel. The high-speed camera focuses on the rigid rake face of the twist drill as the feed motion and

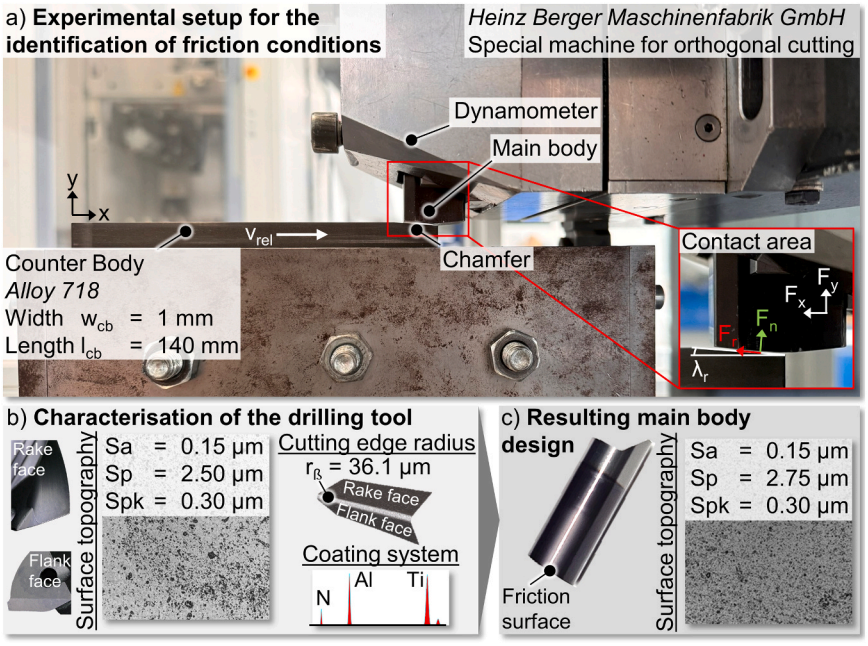

Fig. 7. Development of the main body (c) defined by the surface topography of the drilling tool's flank and rake face (b) and the experimental setup used for discovering the appropriate Coulomb friction coefficient (a).

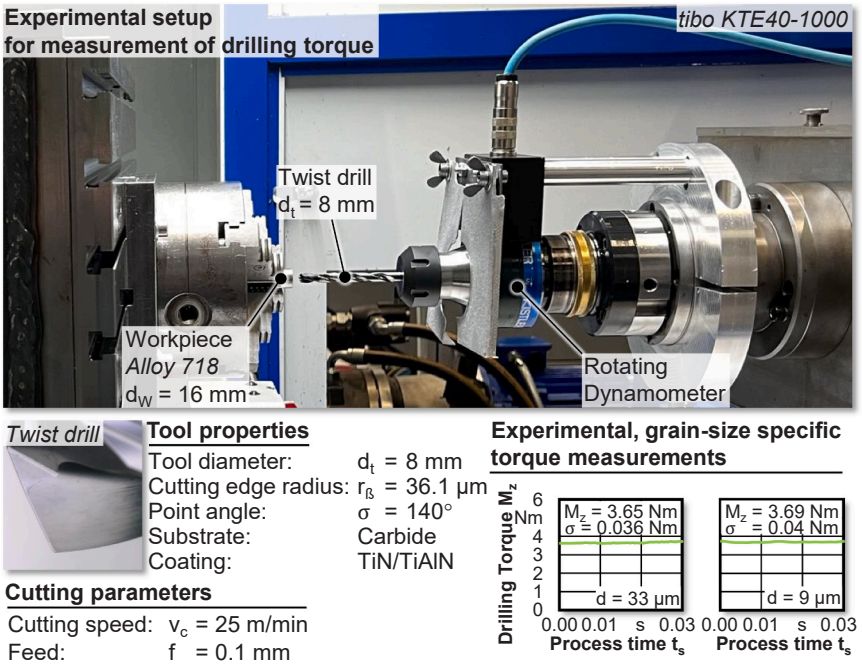

Fig. 8. Experimental setup for analysing the drilling process by measuring the material-specific drilling torque required for validating the simulations. The mentioned standard deviation in force measurements results from the mean value.

cutting speed, aligned with simulated cutting parameters, are executed by the rotating machine spindle. This setup allows for continuous visualisation of chip formation, which can be compared to simulation results, as shown in Fig. 9. It is essential to reduce the specimen diameter to $d_s = 7.5$ mm to prevent radial material flow into the acrylic glass, which would obscure the chip formation zone and the engagement of the cutting tool, which has a diameter of $d_t = 8$ mm.

In conclusion, the methodology for achieving, utilising, and validating the physics-based constitutive models is introduced. This includes material characterisation that revealed different grain sizes and hardness levels, which inform the calibration of flow stress models. Additionally, simulations using these models to calculate the flow stress behaviour of Alloy 718 during chip formation are presented, along with a detailed methodological approach for experimental validation.

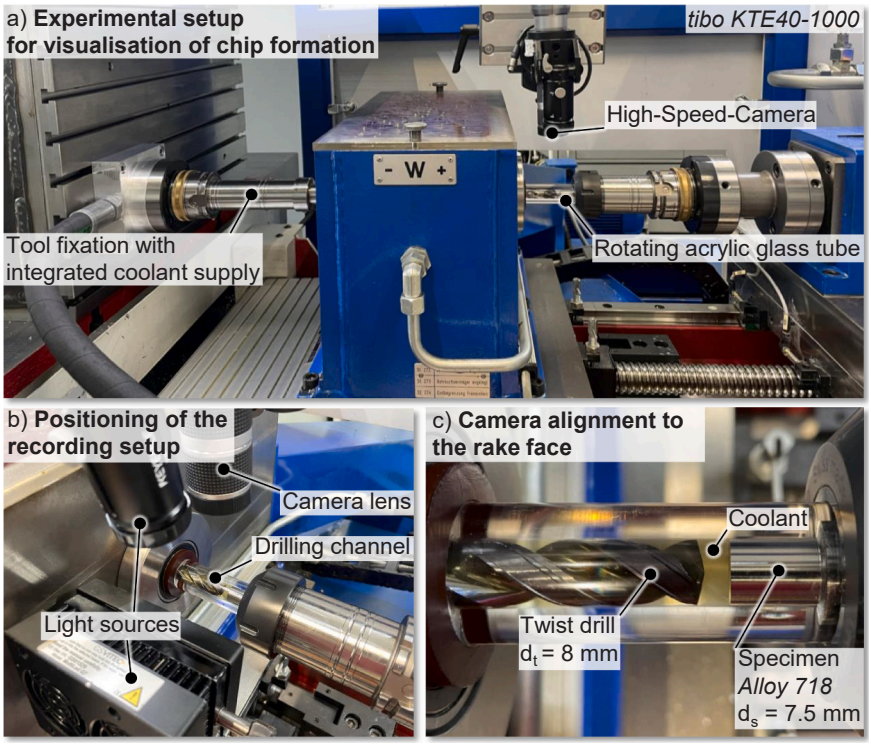

Fig. 9. Experimental setup for visualising the chip formation during drilling of Alloy 718 (a) consisting of a high-speed camera and lighting equipment focusing the drilling channel (b) including the twist drill and the specimen (c).

3. Constitutive modelling of the physics-based flow stress models

A central strengthening mechanism in aged Alloy 718 arises from precipitation hardening effects of γ'' and γ' precipitates [25]. γ'' (Ni_3Nb) with an ordered D022 type body-centred tetragonal (bct) structure and γ' ($Ni_3(Al, Ti)$) with an ordered L12 type structure precipitate coherently in the fcc matrix in this alloy and are referred to as γ phase [26]. The amounts of γ' and γ'' phases are reported to be approximately 4% and 15%, respectively, in peak-aged Alloy 718 [25]. The misfit between the γ'' precipitates and the matrix is also markedly larger than that of γ' [27]. Because of its larger misfit and its relatively larger volume fraction, γ'' precipitates are believed to play a more prevalent role in strengthening Alloy 718 than γ' precipitates. Nevertheless, both solid solution strengthening and precipitation hardening play a substantial role in flow stress properties of Alloy 718; the effect of the latter largely depends on the (Ti+Al)/Nb ratio in a given batch of material [28]. To develop a physics-based flow stress model, the concentration of solute atoms dissolved in the matrix before and after the ageing process, as well as the amount and dimensions of γ' and γ'' precipitates, have to be estimated.

3.1. Thermodynamic and kinetic estimations

The thermodynamic and kinetic calculations based on the well-established CALPHAD phenomenological approaches allow the estimation of the equilibrium concentration of solute atoms at a given temperature, on the one hand, and the determination of the size and volume fraction of the precipitates during the ageing process, on the other hand.

Given the equilibrium concentration of solute atoms in the matrix after the ageing process, i.e., the amount of remaining solute elements not being trapped by γ' and γ'' precipitates, estimating the solid solution strengthening effect based on the extended models for the multi-component systems is possible [29,30]. Moreover, the thermodynamic calculations allow for determining the concentration of the key alloying elements Ti, Nb and Al available for precipitation, and not being trapped by the incoherent δ phase ($Ni_3(Nb, Al, Ti)$) with D0a crystallographic structure stable at the elevated temperatures during the solutionising process. This allows the determination of volume fractions and mean radii of γ' and γ'' precipitates. Consequently, estimating precipitation strengthening in the aged alloy is possible by adopting appropriate models [31], given that the volume fraction and the dimensions of the precipitates remain almost unchanged within the low to medium ranges of temperature (< 873 K).

ThermoCalc® software, along with TCNI8 and MOBNI4 databases, is used in this study to calculate the equilibrium concentrations of the solute atoms Alloy 718 during the solutionising treatment and the amount and size of γ' and γ'' precipitates during and after the double-ageing process. The first step was to estimate the equilibrium phases and concentration of solute atoms in the matrix (γ phase) at the solutionising temperature of 980°C (1253 K). The equilibrium calculations at this temperature resulted in about 94 vol% γ phase, 5 vol% δ phase, about 0.7 vol% (Nb, Ti) C and a slight amount of TiB_2. Fig. 10a shows the equilibrium phases at temperatures ranging from 973 K to 1673 K. The chemical composition of the γ phase at solutionising temperature is summarised in Table 3. This composition is used in the precipitation add-on module to ThermoCalc® software, TC-PRISMA®, to estimate the evolution of size and volume fraction of precipitates during the double-ageing treatment.

TC-PRISMA® incorporates the Kampmann–Wagner numerical (KWN) model of precipitation for concurrent nucleation, growth and coarsening phenomena. The nucleation during the non-isothermal process was taken into account using the model proposed by Jou et al. [32], and the so-called simplified model by Ågren and Chen [33] was adopted to estimate the growth rate of precipitates. Here, γ' is modelled as a spherical particle while γ'' is modelled as a plate (oblate spheroid) with an aspect ratio of 6 [34]. The interfacial energies for γ/γ' and γ/γ'' interfaces are 0.02375 J/m^2 [34,35] and 0.025 J/m^2 [34], respectively. The mean radii and volume fractions of γ' and γ'' after the ageing treatment is shown in Fig. 10b,c, respectively, which are in fair agreement with the estimations made by Zhang et al. [36] and the experimentally measured volume fractions of precipitates for aged-peak Alloy 718 [25]. The kinetic calculations indicate that Nb, Ti, and Al are almost entirely trapped by γ' and γ'' and thus, their concentrations in the matrix (γ phase) are insignificant (Table 3). Hence, only Cr, Fe, and Mo contribute to the solid solution strengthening of Alloy 718 after the double-ageing treatment.

Nevertheless, γ' and γ'' become gradually unstable at elevated temperatures above 600°C (873 K) and 750°C (1023 K), respectively, and

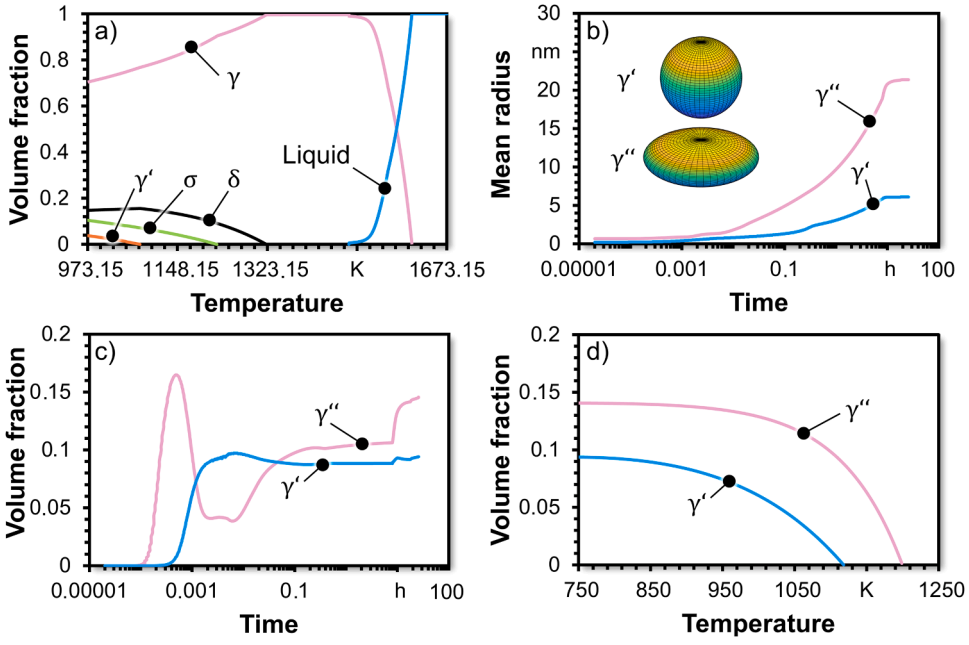

Fig. 10. The equilibrium phases at 1253 K (a), the mean radii (b) and volume fractions (c) of γ' and γ'' after the standard double ageing treatment, the equilibrium volume fractions of γ' and γ'' below their solvus temperatures scaled down according to Semiatin et al. [39] (d).

Table 3
Changes in the chemical composition of the matrix (γ phase) during solutionising and ageing treatment. The alloy composition is provided as a reference.

Condition	Ni	Cr	Fe	Nb	Mo	Ti	Al	C
Alloy composition	Bal.	18.48	18.43	5.35	3.06	0.97	0.59	0.03
After Solutionising	Bal.	19.9	19.7	3.5	3.2	0.7	0.64	0.001
After double-ageing	Bal.	23.2	23.0	0.28	3.8	0.01	0.45	–

dissolve into the γ phase [37]. The dissolution and transformation of these precipitates at elevated temperatures lead to significant flow stress softening, as the precipitation strengthening effect diminishes. The rate at which these phenomena take place during the high temperature and high strain rate processes, such as high temperature SHPB experiments and shear deformation in cutting tests, cannot be estimated readily by the standard kinetic models owing to inherent complexities (e.g., non-equilibrium conditions at extremely short time scales encountered in those processes). Instead, the volume fraction and size of γ' and γ'' precipitates may be approximated under the pseudo-equilibrium condition [38]. To this end, both the dimensions of precipitates (r and t) and their volume fraction (v_p) were corrected in accordance with the equilibrium solvus calculations by Semiatin et al. [39]. This gives the temperature-dependent equations for the volume fraction and radius of the γ' and γ'' with scaling factors below their solvus temperatures under the pseudo-equilibrium condition:

$$\varpi_{\gamma'} = -1.01 \times 10^{-2}\exp\left(4.81 \times 10^{-3}T\right) + 0.5315\exp\left(1.26 \times 10^{-3}T\right) \quad T < 1118\,\mathrm{K} \tag{1a}$$

and

$$\varpi_{\gamma''} = -8.288 \times 10^{-7}\exp(0.01166T) + 0.9382\exp\left(4.143 \times 10^{-5}T\right) \quad T < 1200\,\mathrm{K} \tag{1b}$$

where T is the temperature in Kelvin, while $\varpi_{\gamma'}$ and $\varpi_{\gamma''}$ are the scaling factors adjusting the volume fractions and dimensions of the γ' and γ'', respectively. Note that γ' and γ'' completely dissolve in the matrix (γ phase) at temperatures above 1118 K and 1200 K, as shown in Fig. 10d. It is worth noting that the predictions of the volume fractions and dimensions of γ' and γ'', after double aging process shown in Fig. 10 b and c, are in good agreement with the experimentally measured values reported in the literature [40–42].

3.2. Physics-based constitutive model

Work hardening in metals and alloys results from the continuous generation and movement of mobile dislocations on the slip plane, which is significantly influenced by their interactions with obstacles, including immobile (forest) dislocations, solutes, precipitates, and other defects that impede their movement. The flow stress is expressed additively to account for the various types of interactions [37,43,44]:

$$\sigma = \sigma_0 + \sigma_s + \sigma_{H-P} + \sigma_P + \sigma_G \tag{2}$$

where σ is the flow stress, σ_0 relates to the short-range interactions of the dislocation core structure with the obstacles of various types on the atomic scale. The lattice resistance in pure metals impeding the motion of dislocations and the stress required to overcome the so-called Peierls–Nabarro barriers, formation of sessile dislocation configurations such as Lomer–Cottrell locks, as well as generation of vacancies and self-interstitials due to the reactions between the moving dislocations, are identified as the short-range interactions [45]. σ_s is the solid-solution strengthening effect owing to inclusion of a second constituent into a pure metal, σ_{H-P} is Hall–Petch stress accounting for grain boundary strengthening effects, σ_P is the stress required for mobile dislocations to bow/bypass or shear the nano-size precipitates present in the precipitation hardening alloys, and σ_G is the athermal stress owing to disturbances of the lattice caused, for example, by forest dislocations. In effect, σ_G determines the work hardening rate when straining metals and alloys, relating the flow stress to the density of mobile and/or immobile dislocations. Although there is still no consensus regarding the dominant mechanism governing the flow stress in fcc metals [45], it is well-established that the interaction between the mobile dislocations and obstacles within the glide plane, such as lattice defects, precipitates, and sessile dislocations, poses a considerable barrier to the motion of dislocations. These short-range interactions are believed to play a more critical role in strain hardening than the long-range interactions, such as elastic strain fields generated by the accumulation of primary dislocations on glide planes [46,47].The various terms in the physics-based flow stress model are briefly explored next.

3.2.1. Lattice resistance

The resistance to dislocation glide arises from the periodic distortion of the dislocation core as it moves through the lattice. When a dislocation shifts along the slip plane from its symmetrical position, the misfit energy related to atomic bond separation and restoration oscillates periodically with a period equal to the interatomic separation distance. This energy variation generates a restoring force that anchors the dislocation core to its symmetrical site, inducing resistance to dislocation motion within the lattice [48]. Peierls [49], Nabarro [50], and more recently, Joos and Duesbery [51] determined the magnitude of the lattice resistance at zero Kelvin based on various postulations. The lattice resistance, however, decreases at finite temperatures owing to the thermal assistance over the lattice misfit energy. Following the developments concerning the nature of dislocation glide and plastic deformation, Frost and Ashby [52] derived an equation to estimate the lattice resistance to dislocation motion that can account for the effects of temperature and deformation rate.

Orowan [53] postulated that the dislocation glide is a kinetic process, and the average dislocation velocity on the glide plane can be determined by their waiting time at obstacles. The average velocity of mobile dislocations, with a total density of ρ_m and the Burgers vector b, gliding through a field of obstacles is related to the plastic strain rate by

the following equation:

$$\dot{\bar{\varepsilon}}_p = \frac{\rho_m b \bar{v}}{M} \tag{3}$$

where M is the Tylor factor, which converts the shear strain rates to effective plastic strain rate in this equation, and here, it is taken to be 3.06 (in fcc crystals). The average dislocation velocity may be estimated using the Arrhenius-type equation, provided that the energy barrier that dislocations must overcome to bypass or cut through obstacles such as vacancies and interstitials is known:

$$\bar{v} = \varrho b \nu_\alpha \exp\left(-\frac{\Delta\phi}{kT}\right) \tag{4}$$

where ϱ is a constant, ν_α is the attempt frequency, $\Delta\phi$ is the Gibbs free energy of activation to bypass or cut the obstacles, k is the Boltzmann's constant, and T is absolute temperature. By combining Eqs. 3 and 4, and adopting an appropriate expression for $\Delta\phi$ that accounts for the randomly distributed obstacles in the crystal lattice [54], the stress required for dislocation glide can be estimated as:

$$\sigma_0 = \tau_0 G \left(1 - \left(\frac{kT}{\Delta f_0 G b^3} \ln\left(\frac{\dot{\bar{\varepsilon}}_{ref}}{\dot{\bar{\varepsilon}}_p}\right)\right)^{\frac{1}{q}}\right)^{\frac{1}{p}} \tag{5}$$

where τ_0,Δf_0, q, and p are constants associated with the Gibbs free energy of activation, $\Delta\phi$; while G and $\dot{\bar{\varepsilon}}_{ref}$ are the shear modulus of the matrix (here Nickel) at 0 K and the reference strain rate, respectively.

3.2.2. Solid-solution strengthening

The short-range interaction between the mobile dislocations and solute atoms poses an additional barrier to their mobility in the crystal lattice. Labusch [55], based on a statistical theory, established the link between the stress required for dislocations to move through a random array of solute atoms with a concentration and interaction force between the mobile dislocations and solute atoms in the binary systems containing only two elements. This equation was extended by Gypen and Deruyttere [30] and Toda–Caraballo and Rivera–Díaz–del–Castillo [29] for multicomponent alloy systems with two or more solute elements:

$$\sigma_s = \left(\sum_i B_i^{3/2} c_i\right)^{2/3} \quad ; \quad B_i = ZMG\lambda_i^{4/3} \tag{6}$$

where c_i is the concentration of solute atom i (given in atom fraction), Z is a constant, and λ_i is a parameter that accounts for lattice and shear modulus misfits introduced by the solute atom i:

$$\lambda_i = \xi\left(\bar{\eta}_i^2 + \theta^2 \delta_i^2\right)^{1/2} \tag{7}$$

Here, ξ and θ are the constants related to the number of active slip systems in the lattice structure of the parent phase (matrix) and dislocation type, respectively. $\bar{\eta}_i$ and δ_i are the misfits caused by differences in shear modulus and the lattice parameters of the solute i and the solvent (matrix), respectively. $\bar{\eta}_i$ is given by the following equation:

$$\bar{\eta}_i = \frac{\eta_i}{1 + 0.5|\eta_i|}; \quad \eta_i = \frac{1}{G_{Ni}} \frac{dG_i}{dc_i} \approx \frac{2(G_i - G_{Ni})}{G_i + G_{Ni}} \tag{8}$$

In this equation, G_{Ni} is the shear modulus of the matrix (Nickel in Alloy 718), and G_i is the shear modulus of the solute atom i. The shear moduli of solute/solvent are both taken at 300 K. The lattice misfit is defined as the change in the lattice parameter (a) with the variations in the concentration of solute atoms in solution, and can thus be approximated by:

$$\delta_i = \frac{1}{a_{Ni}} \frac{da_i}{dc_i} \approx \frac{\gamma_{Ni}}{\gamma_i} \frac{r_i - r_{Ni}}{r_{Ni}} \tag{9}$$

where r_i and r_{Ni} are the atomic radii of the solute atom i and Nickel (matrix in Alloy 718), respectively. The parameters γ_{Ni} and γ_i are defined as [29,56]:

$$\gamma_{Ni} = 1 + \frac{4G_{Ni}}{3\kappa_{Ni}} \quad , \quad \gamma_i = 1 + \frac{4G_{Ni}}{3\kappa_i} \tag{10}$$

The solid solution strengthening effect of the key alloying elements in Alloy 718 is calculated using Eq. 6. It is worth noting that only the equilibrium concentrations of Fe, Mo, and Cr dissolved in the γ phase should be used for the calculation of solid solution strengthening after the double-ageing treatment, as mentioned in Section 3.1.

3.2.3. Hall–Petch effect

The grain boundaries also pose a barrier to the movement of the mobile dislocations. With an increase in the density of grain boundaries, a larger energy is required to surpass the boundary layers and change the direction of dislocations into the neighbouring grains. The stress required for the mobile dislocations to overcome the barriers posed by the grain boundaries is well described by the Hall–Petch relationship [39]:

$$\sigma_{H-P} = k_{HP} \frac{G(T)}{G_{Ni}} \frac{1}{\sqrt{d}} \tag{11}$$

where k_{HP} is a constant obtained experimentally and d is the grain size. $G(T)$ and G_{Ni} are the shear modulus of matrix (Ni) at temperature T and room temperature, i.e. 300 K, respectively. The temperature-dependent shear modulus of Ni can be determined as:

$$G(T) = G_{Ni}\left(1 - \beta\left(\frac{T - 300}{T_M}\right)\right) \tag{12}$$

where β is a constant and T_M is the melting point of Alloy 718.

3.2.4. Precipitation strengthening

The stress (σ_P) required for the mobile dislocations to bow/bypass or shear the nano-size precipitates. The oblate (or disc-shaped) γ'' precipitates, formed uniformly in {100} planes, exhibit a stronger strengthening effect compared to γ' precipitates with a smaller volume fraction and a considerably lower misfit with the matrix [25]. Various mechanisms are proposed for precipitation strengthening in Alloy 718. The likely mechanisms discussed in the literature for precipitation strengthening in Alloy 718 comprise chemical strengthening, modulus strengthening, coherency-strain strengthening, atomic order strengthening, and stacking-fault strengthening [26,31,37,57]. Chaturvedi and Han [25], however, showed that the strength of the (under-) aged alloy can be estimated using the combined coherency-strain strengthening effects of γ'' and γ' precipitates. Here, the model proposed by Gerold and Haberkorn [58] is adopted to account for the coherency-strain hardening effect of γ' precipitates. In this model, the γ' precipitates are considered spherical coherent particles characterised by a radius $r_{\gamma'}$ and a volume fraction $f_{\gamma'}$:

$$\sigma_P^{\gamma'} = \Omega MG\left|\varepsilon_{\gamma'}\right|^{3/2} \left(\frac{r_{\gamma'}}{b}\right)^{1/2} f_{\gamma'}^{1/2} \tag{13}$$

where Ω is a constant and $\varepsilon_{\gamma'}$ is the misfit parameter associated with the γ' precipitates. The coherency-strain hardening resulting from the oblate γ'' precipitates impeding the motion of edge dislocations on the glide plane may be estimated based on the model proposed by Oblak et al. [26]:

$$\sigma_P^{\gamma''} = \Phi MG\left|\varepsilon_{\gamma''}\right|^{3/2} \left(t^2 \frac{f_{\gamma''}(1 - \varsigma)}{2br_{\gamma''}}\right)^{1/2} \tag{14}$$

where $r_{\gamma''}$ and t are the radius and half-thickness of the disc-shape (oblate) precipitates, respectively. Φ and ς are constants, and $\varepsilon_{\gamma''}$ is the

misfit parameter associated with the γ'' precipitates. $f_{\gamma''}$ also represents the volume fraction of γ'' precipitates. The combined coherency-strain hardening effect of both precipitates can be estimated using the mean square rule [31]:

$$\sigma_P = \sqrt{\left(\sigma_p^{\gamma'}\right)^2 + \left(\sigma_p^{\gamma''}\right)^2} \tag{15}$$

The crucial step in estimating the precipitation hardening is a reliable calculation of volume fraction and precipitate size (radius and thickness) in the aged material (Section 3.1). Eqs. 1a and 1b are used to scale the volume fractions ($f_{\gamma'}$ and $f_{\gamma''}$) and dimensions ($r_{\gamma'}$, $r_{\gamma''}$, and t) of precipitates in Eqs. 13 and 14 at elevated temperatures.

3.2.5. Strain hardening and recovery

The stress needed for the mobile dislocations to surpass the energy barrier on the glide plane imposed by the extended defects, such as immobile (forest) dislocations, dislocation loops, defect clusters, (sub-) grain boundaries and precipitates, may be estimated by the Taylor equation [59]:

$$\sigma_G = \alpha M G b \sqrt{\rho_i} \tag{16}$$

where ρ_i is the density of immobile (forest) dislocations intersecting the glide plane, and α is a constant typically between 0.2 and 1.1 for metals with an fcc crystal structure [47]. The density of forest dislocation increases when the material is strained. The evolution of forest dislocation density is governed concurrently by (1) the rate at which the primary dislocations on the glide plane are immobilised and (2) the rate at which the immobilised dislocations are annihilated or remobilised. These processes are shown to be temperature and strain-rate-dependent. Immobilisation of dislocations presents new barriers to the movement of the mobile (primary) dislocations on the glide plane, whereas the annihilation of forest dislocations removes the obstacles and thus eases the glide of primary dislocations. The annihilation of forest dislocations during material deformation, a process referred to as dynamic recovery, may be dominated by glide at low and medium temperatures or climb at elevated temperatures through their interactions with vacancies. Hence, the overall evolution rate may manifest in an additive manner, including dislocation storage and annihilation/remobilisation processes:

$$\dot{\rho}_i = \dot{\rho}_i^{(+)} - \dot{\rho}_i^{(-)} \tag{17}$$

where the (+) and (-) notations refer to the storage and annihilation/remobilisation processes, respectively. In general, the rate of dislocation storage depends on the mean free path (Λ) of mobile dislocations, determined by the distribution of the obstacles on the glide plane, for example, (sub-)grain boundaries, cell walls, and solute atoms and precipitates. The rate of dislocation storage can be written as [60]:

$$\dot{\rho}_i^{(+)} = \frac{M}{b}\frac{1}{\Lambda}\dot{\bar{\varepsilon}}_p \tag{18}$$

Here, the dislocation mean free path is assumed to be proportional to the grain size (d), diameter of the dislocation cells (s), and mean distance between the precipitates on the glide plane (l_p). The effects of grain growth and dynamic recrystallisation (DRX) are both neglected in this study; therefore, the grain size is assumed to remain unchanged during material deformation. Furthermore, the diameter of the dislocation cells (or sub-cells and low-energy dislocation structures) is considered to be proportional to the inverse of immobile dislocation density, i.e. $s \propto 1/\sqrt{\rho_i}$ [60]. Accordingly, the inverse of the dislocation mean free path may be described in an additive manner as:

$$\frac{1}{\Lambda} = \frac{k_{grain}}{d} + \frac{\sqrt{\rho_i}}{k_{cell}} + \frac{k_{prec}}{l_p} \tag{19}$$

Here, k_{grain}, k_{cell}, and k_{prec} are the proportionality constants specifying the relative impact of each barrier type on the rate of dislocation storage. Further, if it is postulated that the precipitates lie on a square grid in the glide plane, then the mean distance between them (l_p) may be estimated by [61]:

$$l_p = r_p\sqrt{\frac{2\pi}{3\nu_p}} \tag{20}$$

where r_p and ν_p are the mean radius and volume fraction of precipitates, respectively. Here, it was assumed that $r_p = \left(r_{\gamma'} + r_{\gamma''}\right)/2$ and $\nu_p = f_{\gamma'} + f_{\gamma''}$.

The annihilation/remobilisation of immobile dislocations often happens through a combination of thermally activated phenomena. Nabarro [62] identified the likely mechanisms for dynamic recovery as either cross-slip of dislocations at pre-existing constrictions, climb of dislocations facilitated by the point defects produced during plastic deformation, or the thermally assisted cutting of repulsive immobile (forest) dislocations. In case of the latter mechanism, the probability of annihilation and/or remobilisation of immobile dislocations should, in principle, depend on the frequency at which the mobile and immobile (forest) dislocations encounter on the glide plane. This means that the rate of recovery by dislocation glide is proportional to the densities of both primary and secondary dislocations. The density of primary (mobile) dislocations is directly related to the plastic strain rate based on Orowan postulation (Eq.3), and thus, the rate of recovery by dislocation glide can be estimated as [43]:

$$\dot{\rho}_i^{(-)} = \omega \rho_i \dot{\bar{\varepsilon}}_p \tag{21}$$

where ω is a proportionality constant that typically varies with temperature and rate of deformation.

3.2.6. Stress-update algorithm and model calibration

The radial return algorithm [63] is used in the present study to determine the effective plastic strain increment, given that the one-dimensional stress state prevails in the SHPB test. This algorithm requires the calculation of the yield stress (σ) and hardening modulus to iteratively identify effective plastic strain and the other internal state variable, i.e. density of immobile dislocations (ρ_i). The hardening modulus is defined as:

$$H = \frac{\mathrm{d}\sigma}{\mathrm{d}\bar{\varepsilon}_p} = \frac{\mathrm{d}\sigma}{\mathrm{d}\rho_i}\frac{\mathrm{d}\rho_i}{\mathrm{d}\bar{\varepsilon}_p} \tag{22}$$

The yield stress is calculated using the internal state variables, i.e., effective plastic strain ($\bar{\varepsilon}_p$) and the density of immobile dislocations (ρ_i). The latter can be obtained using a fully implicit approach for a given plastic strain increment ($\Delta\bar{\varepsilon}_p$) and time step ($\Delta t$) by solving Eq. 23 using the Newton–Raphson method:

$$\mathscr{G} = {}^{n}\rho_i - {}^{n-1}\rho_i - \left(\frac{M}{b}\frac{1}{\Lambda}\Delta\bar{\varepsilon}_p - {}^{n}\rho_i\omega\Delta\bar{\varepsilon}_p\right) = 0 \tag{23}$$

where ${}^{n}\rho_i$ and ${}^{n-1}\rho_i - 1$ are the density of immobile (forest) dislocations at iterations n and $n-1$, respectively. Once ρ_i is obtained using Eq. 23, it is then possible to calculate the yield stress using Eq. 2. Tables 4 and 5 summarise the known or estimated parameters and those constants that were determined by model calibration using the SHPB test data. The parameter identification problem was formulated as a constrained minimisation of the global error function using MATLAB's optimisation toolbox. The routine fitted the model to flow curves spanning multiple strain rates and temperatures. The optimisation constraints were selected to restrict the solution space to physically meaningful values consistent with literature data for Alloy 718 [43,44,52,64].

The obtained model, calibrated using experimental SHPB material characterisation, is illustrated in Fig. 11. Additionally, experimental flow stress measurements are included to depict the fitting of experiment and modelling in preparation for transferring the data to the chip formation simulation.

Table 4
Known or estimated parameters.

Parameter	Used in Eq. (No.)	Value	Unit	Comment
k	Boltzmann's constant	1.38×10^{-23}	J/K	
M	Taylor factor	3.06	-	For fcc crystal structure [52]
b	Burgers vector	2.5×10^{-10}	m	For Ni-20 at% Cr alloy [52]
$\dot{\bar{\varepsilon}}_{ref}$	5	10^{6}	s^{-1}	From [52]
${}^{0}\rho_i$	23	5×10^{12}	m^{-2}	Initial density of immobile dislocations
α	16	1	-	Taken as unity in accordance with [47]
ξ	7	1	-	For fcc crystal structure [29]
θ	7	16	-	Taken from [29]
k_{HP}	11	350	MPa$\sqrt{\mu m}$	Taken from [64]
T_M	12	1533	K	Taken from [65]
β	12	0.64	-	For Nickel [52]
r_{Ni}	9	1.3772	Å	Taken from [56]
r_{Cr}	9	1.4205	Å	Taken from [56]
r_{Fe}	9	1.4114	Å	Taken from [56]
r_{Mo}	9	1.5495	Å	Taken from [56]
G_{Ni}	8, 10, 11	80.0	GPa	Taken from [56]
G_{Cr}	8	115.1	GPa	Taken from [56]
G_{Fe}	8	81.4	GPa	Taken from [56]
G_{Mo}	8	125.5	GPa	Taken from [56]
κ_{Ni}	10	183.0	GPa	Taken from [56]
κ_{Cr}	10	160.0	GPa	Taken from [56]
κ_{Fe}	10	169.6	GPa	Taken from [56]
κ_{Mo}	10	261.3	GPa	Taken from [56]
ς	14	0.333	-	Taken from [26]
$\lvert\varepsilon_{\gamma'}\rvert$	13	0.004	-	Taken from [27]
$\lvert\varepsilon_{\gamma''}\rvert$	14	0.0286	-	Taken from [27]
$r_{\gamma'}$	13, 20	6.102×10^{-9}	m	Calculated by TC-PRISMA®
$r_{\gamma''}$	14, 20	21.40×10^{-9}	m	Calculated by TC-PRISMA®
$f_{\gamma'}$	13, 20	0.094	-	Calculated by TC-PRISMA®
$f_{\gamma''}$	14, 20	0.146	-	Calculated by TC-PRISMA®

Table 5
Calibrated parameters using the SHPB data.

Parameter	Used in Eq. (No.)	Value
τ_0	5	6.5×10^{-3}
Δf_0	5	0.43
q	5	2.60
p	5	0.37
Z	6	5×10^{-3}
Ω	13	2.0
Φ	14	1.5
k_{grain}	19	0.001
k_{cell}	19	190
k_{prec}	19	2×10^{-4}
ω	21	6.5

4. Results

To discuss the application of a physics-based constitutive model, two-dimensional simulations of orthogonal cutting and three-dimensional simulations of the drilling process were performed and compared to experimental data. Preliminary, specific experimental work was conducted to identify the friction conditions in the contact zone at the rake face of the twist drill. Thus, a qualified friction setting for the simulations can be achieved.

4.1. A qualified friction setting for three-dimensional chip formation simulations

The introduced experimental setup enables the analysis of the prevailing friction conditions at the interface between the chip and the rake face, as well as at the interface between the recently cut surface and the flank face. For conducting the experiments, an infeed of the main body of $a_r = 0.15$ mm was set up to achieve contact when the relative motion with a speed of $v_{rel} = 15$ m/min is initiated. Owing to the inclination of $\lambda_r = 5°$, a friction speed of $v_r = 14.94$ m/min is obtained. Because of the actuated motion, the component contact builds up and a contact length of $l_r = 1.72$ mm develops; here, friction-related signs of wear are observed, as shown in Fig. 12a. In addition, Fig. 12b at the top right shows a single frame from a high-speed video of the friction test and the arrangement of the normal and friction forces in relation to the position of the bodies. The lower figure shows time records of the two force components and the coefficient of friction resulting from the force ratio.

Combined with the width of the counter body, a specific contact area is formed, which can be calculated to derive the stresses from the measured forces. As previously discussed, the measured force data can be converted into friction and normal forces. To derive an adequate Coulomb friction model with a well-fitting apparent friction coefficient, a constant interval of the measurement plot is defined for $\Delta t_p = 0.045$ s starting at $t_p = 0.35$ s, like illustrated in Fig. 12. This time period is characterised by consistent and uniform graphs qualified to calculate the averaged normal force to $F_{n,avg} = 1709$ N and the averaged friction force to $F_{r,avg} = 676$ N. Considering the determined contact area, this yields a normal contact stress of $\sigma_N = 907$ MPa and a friction stress of $\tau_f = 359$ MPa. Compared to the stresses determined by Puls et al. [23], the Coulomb model can be assumed to be still applicable to a large extent in this stress range for Alloy 718 under the given boundary conditions. In accordance with the definition of the Coulomb friction model, these forces and stresses are related, resulting in an averaged value of $\mu_{avg} = 0.4$ for a relative speed of $v_r = 14.94$ m/min.

In summary, the detailed experimental analysis enabled the characterisation of a representative apparent friction coefficient under cutting-like conditions on a surface replicating the topography of the twist drill's coating. Based on these findings, a Coulomb-type sliding friction model is employed in the subsequent numerical chip formation simulations to represent, in an aggregated manner, the dominant mechanisms occurring at the frictional interface. The performance of the selected apparent friction coefficient is discussed in comparison to applying the more complex friction model taken from [20].

4.2. Application of physics-based flow stress models in two-dimensional simulations

The comparison of two modelling approaches for describing the flow stress behaviour of the nickel-based Alloy 718 in chip formation simulation is initially performed in a 2D orthogonal cutting configuration as illustrated in Fig. 4. The state of the art reference simulation was performed with a Johnson–Cook flow stress model developed by Malakizadi et al. [20] for a workpiece with an average grain size of $d = 16$ µm. Similar simulations were subsequently performed incorporating the newly calibrated physics-based constitutive models. The associated flow stress properties were generated for the materials with identified grain sizes of $d = 9$ µm and $d = 33$ µm, corresponding to the minimum and maximum values measured in this study. This is because the deformation behaviour of the material with $d = 15$ µm is expected to lie within this range, given that the chemical composition and heat treatment condition were similar, and thus the size and amount of hardening precipitates.

Fig. 13 presents the simulation results for a cutting speed of $v_c = 30$ m/min, including the cutting and tangential force, the contact length, the chip thickness, and the shear angle in comparison to the experimental data.

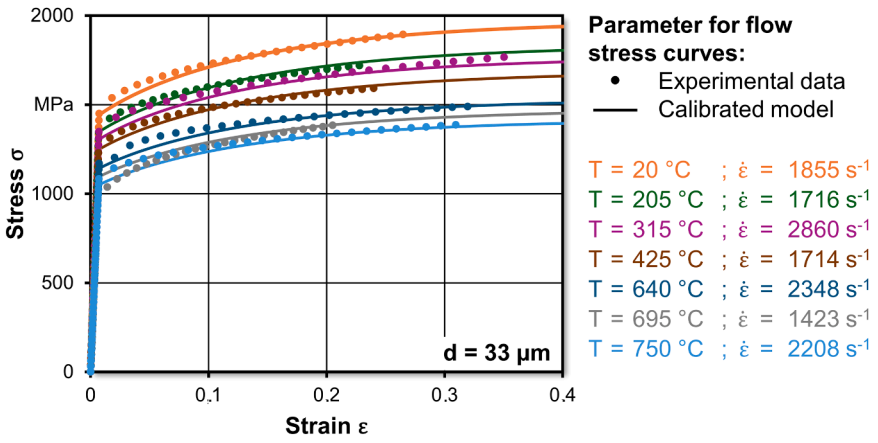

Fig. 11. Calibrated model (solid lines) and its comparison with the experimental flow stress measurements using SHPB (dots).

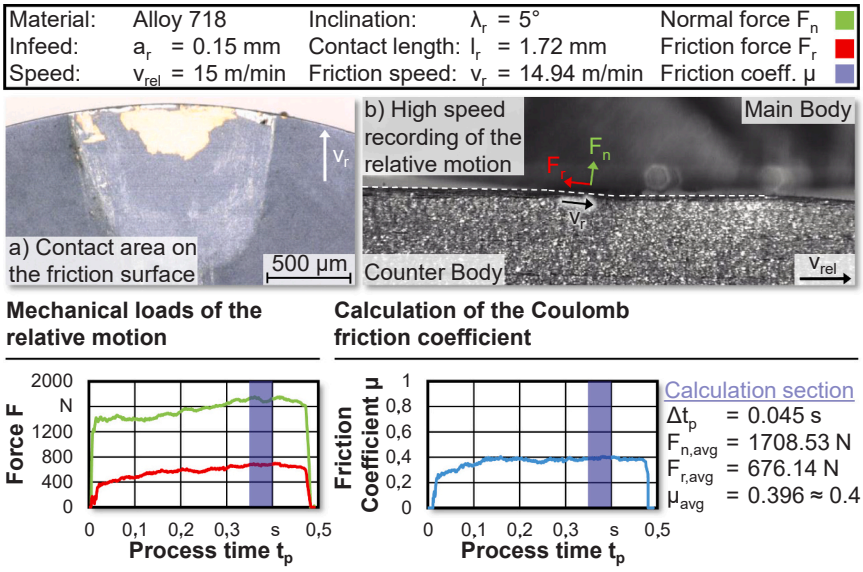

Fig. 12. Experimental approximation of the relative motion in the secondary shear zones of the drilling process resulting in a Coulomb friction coefficient. The contact area of main and counter body (a) illustrates the relative motion documented by the high-speed recordings (b). The simultaneously recorded mechanical loads were transferred into a Coulomb friction coefficient to be used in the numerical work.

The analysis of the presented results allows for a detailed insight into the numerical behaviour of the developed physics-based constitutive models in comparison with the adopted Johnson–Cook flow stress model. Concerning the mechanical tool loads, it can be stated that the reference simulation in Fig. 13a results in a cutting force of $F_c = 348$ N, which implies a deviation to the experimental data from [20] amounting to $\Delta_{exp\ ,JC16} = -4.4\%$. In comparison, the highest deviation resulting from the application of the physics-based flow stress models occurs for the one of a grain size $d = 9$ µm in Fig. 13c, constituting in $\Delta_{exp\ ,PB9} = 5.5\%$ while the lowest deviation of $\Delta_{exp\ ,PB33} = 3.9\%$ is documented for the physics-based model calibrated for a microstructure with an averaged grain size of $d = 33$ µm (Fig. 13b). All three results are within the range of high predictive accuracy.

The calculated contact length when using the Johnson–Cook flow stress model of Alloy 718 with a grain size of $d = 16$ µm results in a deviation to the experiments of $\Delta_{exp\ ,JC16} = -44.6\%$. By applying the physics-based model with a grain size of $d = 9$ µm, the error is reduced to $\Delta_{exp\ ,PB9} = -28.9\%$ and the contact length consequently increases, accompanied by higher cutting forces. However, the highest maximum effective stresses of $\sigma_{eff,max} = 1990$ MPa are predicted by the Johnson–Cook model.

These findings can be attributed to the different shear angles identified in the respective simulations, which exert a considerable impact on the stress conditions. Whereas the shear angle in the reference simulation is measured to $\Phi = 26.9°$ when using the Johnson–Cook flow stress model, it can be specified as $\Phi = 21.7°$ for the physics-based models considering grain sizes of $d = 33$ µm and $d = 9$ µm, respectively. In this context, a reduction to $\sigma_{eff,max} = 1780$ MPa and $\sigma_{eff,max} = 1850$ MPa can be stated. Additionally, the reduction in shear angle observed when applying the physics-based flow stress model affects the resulting chip thickness, leading to an overestimation of $\Delta_{exp\ ,PB33} = 52.5\%$ and $\Delta_{exp\ ,PB9} = 49.1\%$, respectively. In contrast, the simulation using the Johnson–Cook model predicts the chip thickness with an error of $\Delta_{exp\ ,JC16} = 8.5\%$, demonstrating the closest agreement with the experimental data.

The calculation of the tangential forces completes the analysis, revealing a comparable force level across the investigated simulations.

The analysis of the two modelling approaches is extended to a cutting speed of $v_c = 60$ m/min, and the corresponding results are presented in Fig. 14. Those are again predominantly determined by the simulated shear angle. While the application of the Johnson–Cook model results in a shear angle of $\Phi_{JC16} = 32.2°$, the physics-based constitutive models

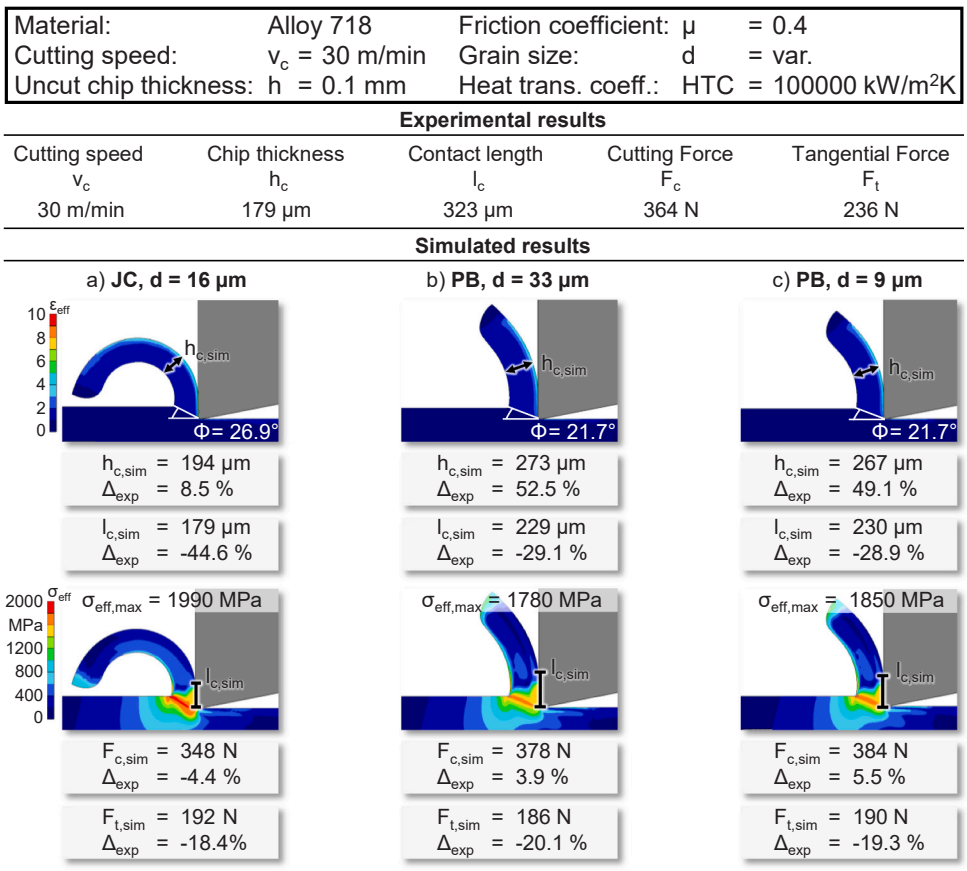

Fig. 13. 2D simulations with a cutting speed of $v_c = 30$ m/min were performed to evaluate the performance of the calibrated physics-based models representing material with a grain size of $d = 33$ µm (b) and $d = 9$ µm (c) in comparison with the baseline Johnson–Cook model with $d = 16$ µm (a).

predict reduced values of $\Phi_{PB33} = 24.1°$ and $\Phi_{PB9} = 24.4°$, respectively. Consequently, this reduction shows impact on the analysed process responses. In particular, the accuracy of calculated contact length is enhanced and the error of $\Delta_{exp,JC16} = -38.6\%$ for using the Johnson–Cook model is reduced to $\Delta_{exp,PB33} = -19.6\%$ and $\Delta_{exp,PB9} = -21.5\%$, respectively. As a further result of the reduced shear angle, the chip thickness increases when using the physics-based models and is consistently overestimated in comparison to the experimental results. In contrast to the improved prediction of the contact length, the deviation of $\Delta_{exp,JC16} = 12.3\%$ intensifies to $\Delta_{exp,PB33} = 53.4\%$ and $\Delta_{exp,PB9} = 50.7\%$. Regarding the analysis of cutting forces, an underestimation of $\Delta_{exp,JC16} = -3.6\%$ is observed in the 2D chip formation simulation using the Johnson–Cook flow stress transitions to an overestimation of $\Delta_{exp,PB33} = 5.8\%$ and $\Delta_{exp,PB9} = 7.4\%$ when the physics-based models are applied. The contact length also shows influence on the tangential forces because the lower tool-chip interface compensates the increased stresses, which are identified for the simulation using the Johnson–Cook flow stress model.

The comparison of the selected flow stress models applied in the chip formation simulations of orthogonal cutting is carried out using the previously calibrated friction model with the apparent friction coefficient from experimental work. This approach constitutes a simplified representation of the complex mechanisms governing the frictional contact. Consequently, the simulation outcomes based on this formulation requires additional validation.

Accordingly, the results of a brief study on the variation of the friction model in comparison with experimental measurements are shown below. This study compares the adapted Coulomb model with a pressure-dependent shear friction model from [20], the formulation of which takes into account the fact that the contact is divided into a sliding zone and a sticking zone. Fig. 15 shows the prediction of mechanical tool loads in orthogonal cutting using the constant apparent friction coefficient and the complex friction model, respectively. For validation, the same experimental data as previously reported in [20] are used.

For the simulation of orthogonal cutting at a cutting speed of $v_c = 30$ m/min, improved predictions of the cutting force are obtained with both physics-based flow stress models, when a constant apparent friction coefficient is implemented. Accordingly, for the physics-based flow stress model representing a grain size of $d = 33$ µm, the deviation from the experimental cutting force is reduced from $\Delta F_{c,PB33,\alpha} = 13.5\%$ to $\Delta F_{c,PB33,\mu} = 3.9\%$. For the grain size of $d = 9$ µm, the deviation is likewise reduced from $\Delta F_{c,PB9,\alpha} = 15.9\%$ to $\Delta F_{c,PB9,\mu} = 5.5\%$. However, it has to be stated, that the numerical estimation of tangential force is more accurately represented by the simulation using the pressure-dependent shear friction model. Hence, a deviation of $\Delta F_{t,PB33,\mu} = -21\%$ and $\Delta F_{t,PB9,\mu} = -19.3\%$ is compared to $\Delta F_{t,PB33,\alpha} = 6.8\%$ and $\Delta F_{t,PB9,\alpha} = -5.5\%$. Increasing the cutting speed to $v_c = 60$ m/min leads to convergent behaviour of the simulations, resulting in comparable deviations. With respect to the cutting force, the deviations for the Coulomb-type friction model amounts to $\Delta F_{c,PB33,\mu} = 5.8\%$ and $\Delta F_{c,PB9,\mu} = 7.4\%$, whereas values of $\Delta F_{c,PB33,\alpha} = 9.4\%$ and $\Delta F_{c,PB9,\alpha} = 10.3\%$ are obtained when applying the complex friction model. Evaluation of the tangential forces reveals errors of $\Delta F_{t,PB33,\mu} = -3.8\%$ and $\Delta F_{t,PB9,\mu} = -1.6\%$ for using an apparent friction formulation while the complex model yields deviations of $\Delta F_{t,PB33,\alpha} = 4.7\%$ and $\Delta F_{c,PB9,\alpha} = 4.7\%$. These results indicate that the complex friction model used by Malakizadi et al. [20], which accounts for dynamically varying pressure conditions, does not provide a consistent advantage over the apparent Coulomb-type friction formulation. While assuming sliding friction already provides superior prediction accuracy for the cutting forces at relatively low cutting speeds, the discrepancies regarding tangential force prediction is clearly improved for increased cutting speeds.

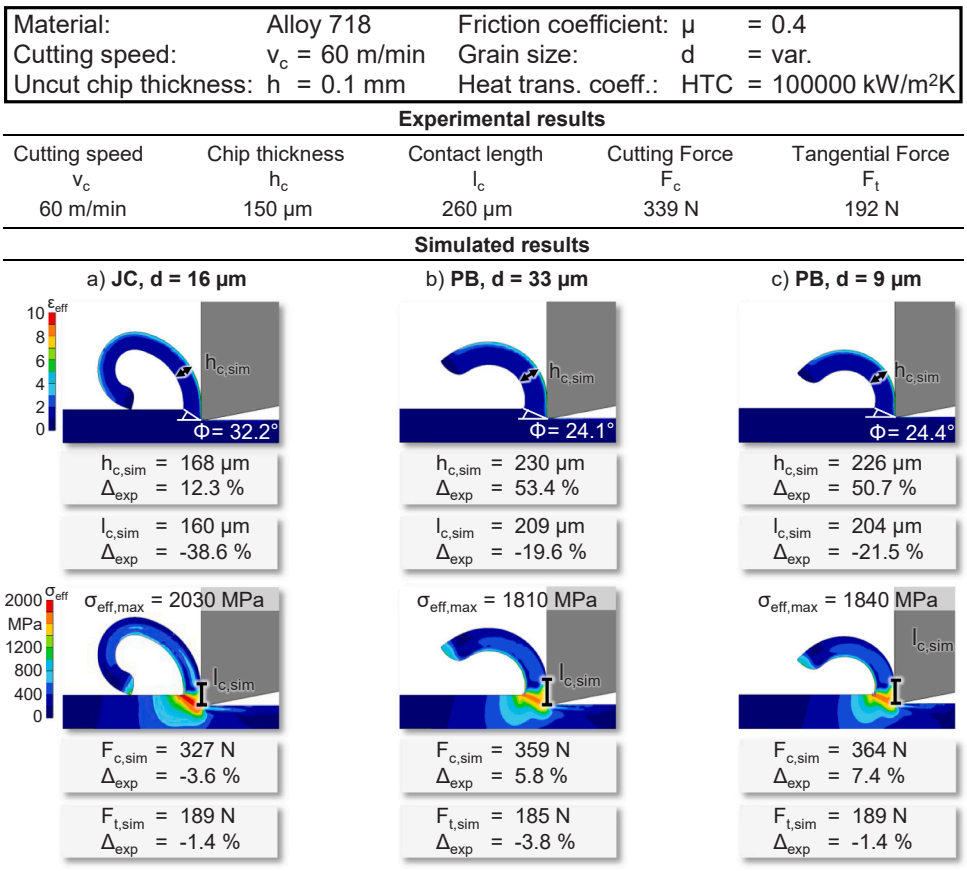

Fig. 14. 2D simulations with a cutting speed of $v_c = 60$ m/min were performed to evaluate the performance of the calibrated physics-based models representing material with a grain size of d = 33 µm (b) and d = 9 µm (c) in comparison with the baseline Johnson–Cook model with $d = 16$ µm (a).

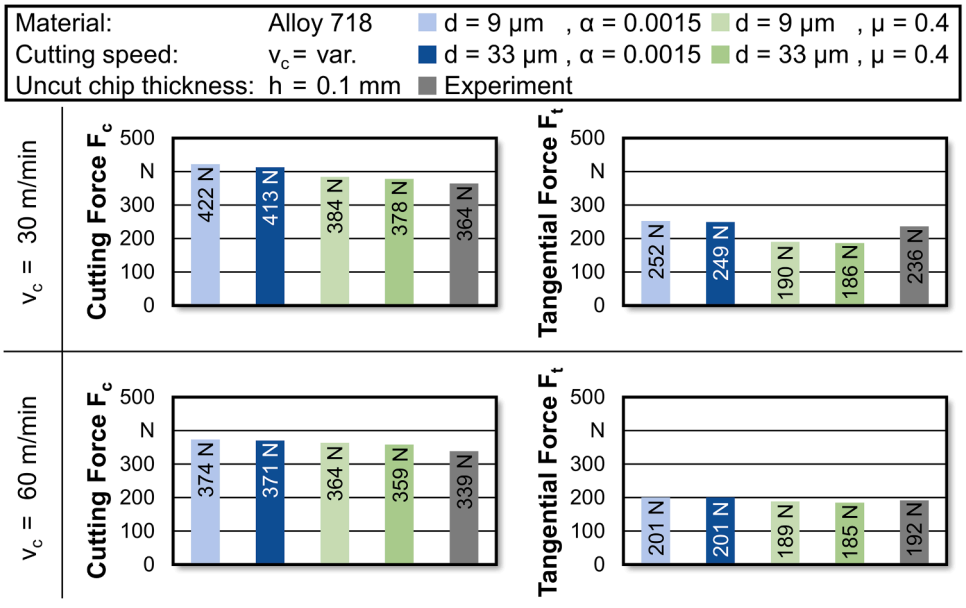

Fig. 15. Mechanical tool load predictions for varying friction models in 2D chip formation simulations.

4.3. *Three-dimensional simulations of chip formation in a drilling process*

To analyse the influence of physics-based constitutive models, three-dimensional simulations designed to model chip formation in drilling Alloy 718 are provided with specific flow stress data generated for the workpiece material with the grain sizes of $d = 33$ µm and $d = 9$ µm, respectively.

4.3.1. *Comparison of mechanical tool load*

For two of the identified grain sizes, the derived physics-based constitutive models were used with boundary conditions of the observed drilling process to enable a comparison with the

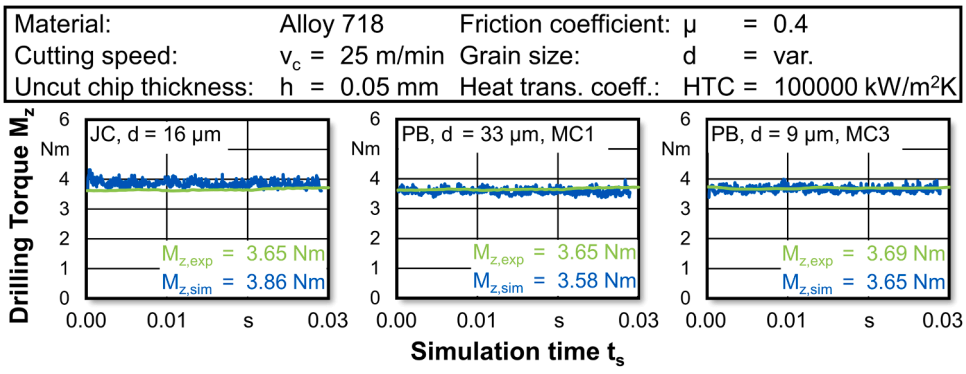

Fig. 16. Comparing the 3D drilling simulation results for using the Johnson–Cook (JC) flow stress model (a) as well as the physics-based (PB) models (b + c) in combination with a friction coefficient μ = 0.4.

Johnson–Cook reference model. Fig. 16 displays the resulting drilling torque from the particular simulation in contrast to the experimental data for machining materials with the corresponding grain size. Regarding the Johnson–Cook model, a deviation in drilling torque of $\Delta M_{z,JC16}$ = 5.38% can be stated, which already represents a good agreement with the experimental data. However, the application of the physics-based constitutive models shows an even smaller absolute deviation of $\Delta M_{z,PB33}$ = -1.86%, which can be attributed to the implementation of the constitutive model derived from a grain size of d = 33 µm. The results of drilling simulations of Alloy 718 with a grain size of d = 9 µm reveals a deviation of $\Delta M_{z,PB9}$ = -0.88% in contrast to the experimental drilling torque.

The acquired torque for the experimental drilling of material with a grain size of d = 33 µm results in $M_{z,exp,PB,33}$ = 3.65 Nm. The evaluation of mechanical tool loads for the drilling of Alloy 718 with a microstructure defined by a grain size of d = 9 µm showed a drilling torque of $M_{z,exp,PB,9}$ = 3.69 Nm. The simulation of these processes follows this tendency, and the marginal variation is reproduced with a drilling torque of $M_{z,sim,PB,33}$ = 3.58 Nm and $M_{z,sim,PB,9}$ = 3.65 Nm.

4.3.2. Simulation analysis of chip flow velocities

To reinforce the plausibility of defining the friction coefficient to μ = 0.4 arising from the preliminary experimental work, the simulations are additionally analysed regarding the prevailing chip flow speeds in the contact of chip and rake face, as the experimental characterisation was aimed at fitting the average relative speed in the drilling process and consequently, map an adequate friction behaviour in the simulations. Thus, the contact area of the tool and workpiece in the particular simulations is examined and discretised in the direction of the depth of cut, which is defined by the width of the cutting edge. In accordance with the gradient of cutting speed in this direction, the chip flow speeds increase simultaneously, as shown in Fig. 17 for two different flow stress models. Regarding the simulation using the Johnson–Cook model, the average chip flow velocity in the secondary shear zone is $v_{ssz,JC16}$ = 13.86 m/min and $v_{ssz,PB9}$ = 14.07 m/min for the simulation using the physics-based constitutive model.

This reduction in the average chip flow speed compared to the cutting speed of v_c = 25 m/min results from material compression in the primary shear zone, leading to increased chip thicknesses compared to the uncut chip thickness. The discovered values are in good agreement with the friction speed of v_r = 14.94 m/min that was defined for the experimental friction characterisation. The performed analysis of the chip flow speed confirms the quality of the chip formation simulation describing the drilling of Alloy 718 using the selected Coulomb friction model with an apparent friction coefficient of μ = 0.4, representing sticking and sliding frictional conditions simultaneously.

4.3.3. Comparison of chip morphology

Based on the analysis of the drilling torque occurring in grain-size-dependent simulations, the numerical chip morphology in the drilling of Alloy 718 is considered for evaluating the application of constitutive flow stress models. Fig. 18 presents the visualisation of the actual chip

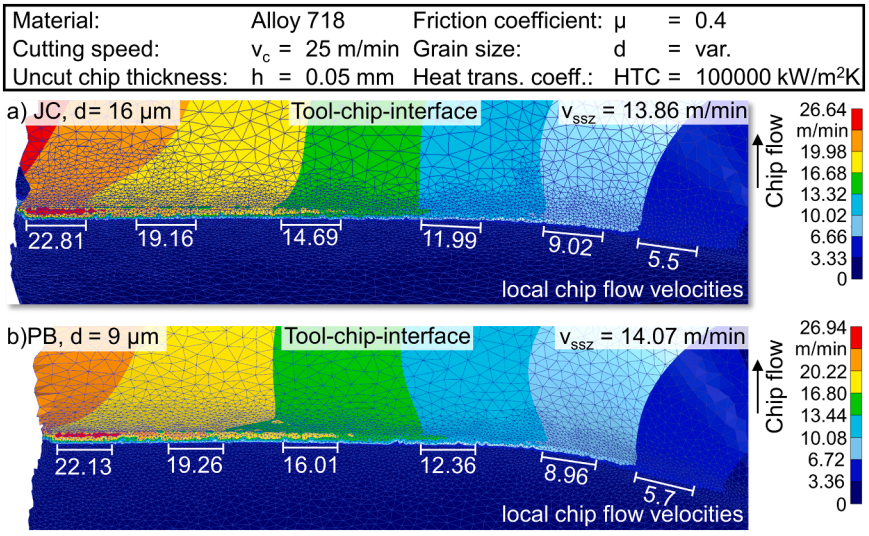

Fig. 17. Analysis of simulated chip flow velocities when using a Johnson–Cook flow stress model (a) and a physics-based flow stress model (b) with a constant Coulomb friction coefficient μ = 0.4 in order to verify its experimental determination.

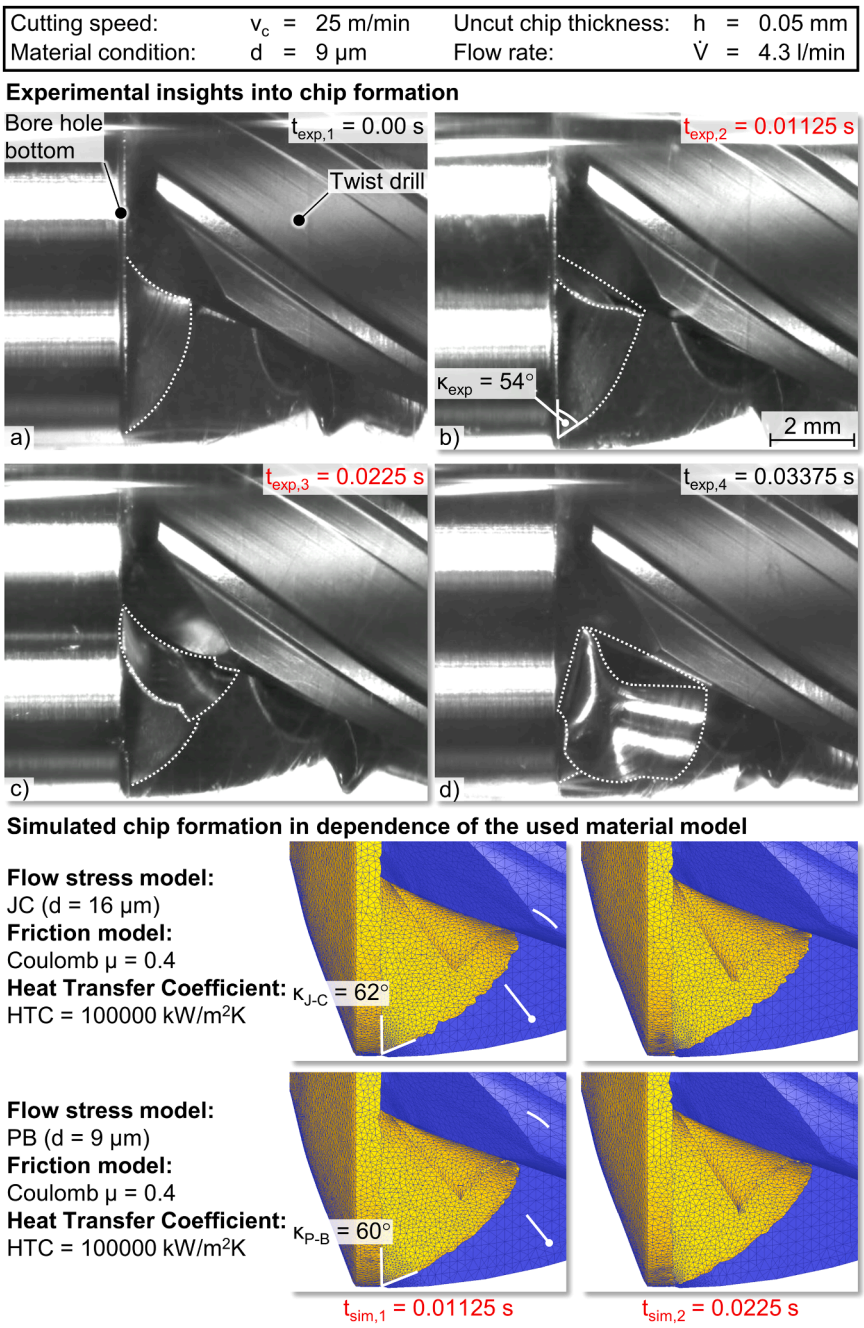

Fig. 18. Visualisation of chip formation (a – d) and comparison to the performed 3D simulations (e – h).

formation for the drilling experiments (upper part) and the chip formation simulations (lower part) for a detailed comparison and evaluation of the simulation work. Due to the facts, that the specimen prepared for the conducted experiments were extracted from Alloy 718 present in MC3 and the numerical work resulted in a similar force level of MC3 and MC1, the analysis of chip formation is focused on opposing the experimental data to the simulation of the Johnson–Cook reference model derived from material with an average grain size of $d = 16$ µm (Table 2) and the physics-based constitutive model evolved from the material with a grain size of $d = 9$ µm. During the tool engagement, the chip develops with an inwardly directed curvature owing to the cutting speed gradient, which becomes visible in Fig. 18a at $t_{exp,1} = 0.00$ s, representing the beginning of the analysis. Owing to centripetal forces, the material tends to flow preferentially towards the centre of the twist drill, where the speeds are lower than at the cutting edge corner. At the outer corner, where the speed is at its maximum and corresponds to the set cutting speed, the chip completely falls off. In the following, the chip flows along the rake face contour, and as a result, curling is initiated (Fig. 18b) at $t_{exp,2} = 0.01125$ s. In Fig. 18c at $t_{exp,3} = 0.0225$ s, the chip morphology is already significantly influenced by the curling. With ongoing chip flow in Fig. 18d at $t_{exp,4} = 0.03375$ s, corresponding with the time approximately needed for half a tool rotation, the chip reaches a critical length and consequently collides with the chip flute wall, which serves as an interference contour leading to a bending load that, combined with the pre-damage to the material, causes the chip to break. As can be seen in the frame, the chip detaches from the material bond and begins to move with the flow of the cutting fluid. This procedure of chip formation and breaking is characteristic of drilling processes using twist drills.

The points in time $t_{exp,1}$ and $t_{exp,2}$ are selected for comparison with

the simulated chip formation (lower part of Fig. 18), and their characteristic shape is well represented. The analysis in $t_{sim,1} = 0.01125$ s and $t_{sim,2} = 0.0225$ s indicates that the simulations are both capable of qualitatively reproducing the described chip formation and the mentioned material flow into the chip flute. Nevertheless, small deviations regarding the particular material flow in chip formation of experiments and simulations can be identified and quantified accordingly by analysing the described curvature of the chip. During the experimental chip flow, the angle of curvature related to the contour of the bore hole bottom is defined as $\kappa_{exp} = 54\ ^\circ$. The numerical calculation yields a curvature angle of $\kappa_{JC} = 62\ ^\circ$ when using the Johnson–Cook reference and $\kappa_{PB} = 60^\circ$ when the flow stress calculation is based on the physics-based constitutive model. This angle, which is significantly larger than that in reality, and consequently the steeper rise of the edge of the chip from the outer corner towards the centre of the borehole, indicates less compression of the chip and hence, a lower chip thickness than in reality. The flow stress models, therefore, probably overestimate the plastic flow resistance of the material.

5. Discussion

Within the framework of two-dimensional simulations of orthogonal cutting and three-dimensional simulations of drilling Alloy 718, the implementation of physics-based flow stress models using SHPB data and incorporating the applied heat treatment was investigated in order to assess their predictive capability in comparison with a high-quality Johnson–Cook model. In the first part of the analysis, the conducted two-dimensional orthogonal cutting simulations demonstrated high accuracy in predicting key process responses, including cutting forces, contact length, and chip thickness. The Johnson–Cook flow stress model already showed a satisfactory prediction of chip formation. However, the application of the physics-based models derived from the executed material characterisation exhibited a comparable level of predictive performance when evaluated against the experimental data used for calibration of the Johnson–Cook flow stress model. This similarly high level of predictive accuracy is remarkable because, unlike the JC model, a completely different dataset was used for calibrating the physics-based models than for validating them, which places significantly greater demands on the model's interpolation and extrapolation capabilities. The approach taken for the Johnson-Cook model was deliberately chosen to obtain a reference with strong predictive power.

These results can primarily be attributed to the ability of the physics-based models to account for thermal softening, dynamic recovery, and strain-rate sensitivity in Alloy 718, in contrast to the Johnson–Cook modelling approach. As a result, discrepancies in the predicted shear angle occur, a critical parameter controlling chip thickness and thereby influencing contact length and cutting forces. The higher shear angle of $\Phi = 26.9^\circ$ for the Johnson–Cook model in the simulation of a cutting speed of $v_c = 30$ m/min results in correspondingly increased stress conditions orthogonally to the cutting direction with impact on the tangential forces. Because the Johnson–Cook model does not account for dynamic recovery, the predicted stress increases unboundedly with increasing strain. In contrast, the physics-based models incorporate dynamic recovery, leading to a convergence of flow stress toward a steady-state with increasing strain. The observed lower level in the prevailing stresses, which was stated for the physics-based flow stress models, is compensated by the lower shear angle which results in higher chip thickness and higher contact length at the rake face. Further simulations performed at a cutting speed of $v_c = 60$ m/min using varying flow stress models corroborate the previously discussed findings by once again highlighting the refined prediction of the shear angle and its impact on the associated process responses. The described interaction of shear angle, contact length, and chip thickness affects the tool loads in the cutting direction.

Consequently, the subsequent evaluation of the flow stress models under three-dimensional conditions, characterised by increased complexity of multiaxial strain and stress states, substantiates the limitations of the Johnson–Cook approach while simultaneously highlighting the advantages of the physics-based flow stress models: Using the latter lead to a significantly better prediction of the drilling torque. Whereas the proposed physics-based formulation demonstrates robust adaptability to varying cutting conditions, the transfer of the Johnson–Cook model to the simulation of the drilling process underscores its dependency on inverse calibration and highlights its systematic inability of accurately reproduce intrinsic material behaviour, such as thermal softening, as also reported in the literature [66]. In contrast, the physics-based constitutive models are capable of accurately capturing this effect, further accounting strain rate sensitivity and provide an enhanced representation of the dynamic recovery process, resulting in an improved prediction of the stress plateau at large strains – phenomena that Johnson-Cook material model fails to predict.

Yet, it has to be mentioned that the analysis of the simulation results indicates that the Johnson–Cook model overpredicts the drilling torque, while the physics-based models exhibit a slight tendency towards underestimation. This behaviour, in contrast to that observed in the 2D simulations, can likely be explained by the generally reduced cutting speed of $v_c = 25$ m/min and the correspondingly varying ranges of strain rate as well as from the calculation of the torque over the three-dimensional contact area, accounting for the prevailing cutting speed gradient that was visualised in the simulation results. Furthermore, it has to be considered that the estimation of stresses and strains transitions from a plane strain condition to a three-dimensional state and consequently, the calculation of drilling torque is affected. Nevertheless, the results clearly substantiate the performance advantage of the proposed models over the reference formulation.

Beyond the actual methodological approach of calibration, the procedure of generating the experimental input data, a central requirement of advanced flow stress models, differs. In contrast to the inverse calibration of the Johnson–Cook model performed by Malakizadi et al. [20], which was based on the results of using one specific orthogonal cutting experimental setup, the physics-based constitutive models in the present study were derived from the described SHPB data to overcome the limitation to one particular cutting condition. Thus, a comprehensive characterisation of the flow stress behaviour is achieved. Nevertheless, even when adhering to this methodological principle, minor deviations in chip formation persist, which can be attributed to the strain and strain rate levels achievable in SHPB experiments, as these remain substantially below those occurring in actual cutting processes. Moreover, in contrast to the dominant shear strains characteristic of machining, which represent the foundation of calculating process forces focused on inverse calibration, the design of physics-based constitutive models is based on unidirectional loading conditions. Consequently, the extrapolation to the substantially higher strains and stresses occurring during chip formation is essential and critically determines the predictive capability of the model. Further developments are required to overcome this deficiency by developing a hybrid approach that combines the SHPB data with inverse modelling of orthogonal cutting process – similar to the approaches by Malakizadi et al. [67] and Shi et al. [68] – to account for high strains and strain rates encountered in the cutting process. Such hybrid approaches are shown to improve the reliability of the calibrated models for cutting simulations regardless of the model being implemented.

For the hybrid calibration approaches to be effective, the priori knowledge of friction model for simulation of orthogonal cutting is vital. An apparent friction coefficient derived from experimental investigations of the relative motion between Alloy 718 workpieces and specific tools replicating the topography of twist drills used in the subsequent analyses was compared with a complex pressure-dependent friction model. The results in 2D already demonstrate that the simplified friction formulation is suitable for numerical chip formation simulations. Owing to its experimental derivation under friction conditions representative of the chip formation zone, its implication within the

investigated 3D simulation framework is well justified. Consequently, the comparison of the flow stress models in the drilling simulations focuses on the application of a Coulomb-type friction model defined by an apparent friction coefficient taking into account both sliding and sticking contributions. Thus, the chip formation simulations are conducted using a well-established methodological approach [69,70]. However, this assumption reflects a methodological simplification and should be critically reassessed in the course of future friction model development.

In summary, the validated physics-based constitutive model presented in this study serves as the foundation for developing more advanced flow stress models of nickel-based alloys under various heat treatment conditions. These models will facilitate accurate chip formation simulations, which are critical for process development in industries such as aerospace, thereby enhancing predictions of thermomechanical tool loads and workpiece microstructure. To improve upon the experimentally determined constant friction coefficient, the chip formation simulation has to incorporate a differentiated friction model that accounts for the effects of relative speed and temperature on friction conditions.

6. Conclusions

This study presents a physics-based constitutive model to describe the flow stress of Alloy 718 in numerical drilling simulations. It explains the fundamental material characterisation and the transformation into microstructure-adaptive models. The results from initial 2D simulations and subsequent 3D chip formation simulations using these models are discussed and compared to reference simulations using Johnson–Cook flow stress models. Finally, we critically assess the ability of different drilling models to represent real chip formation behaviour, focusing on mechanical tool loads and chip morphology. The following insights and findings can be concluded:

(1) A physics-based model is developed to account for the effect of grain size as well as the size and amount of γ' and γ'' phases. The developed model includes the effects of various deformation mechanisms, including solid solution strengthening, grain boundary strengthening, and precipitation hardening. Combined with CALPHAD-based thermodynamic and kinetic simulations, this model enables the prediction of flow stress properties of Alloy 718 with a specific chemical composition and microstructural characteristics over a wide range of strain rates and temperatures.

(2) The modelling and calibration procedures of physics-based flow stress models highlight significant advantages over phenomenological models. With knowledge of the heat treatment and chemical composition of a material, an adaptive dislocation-based flow stress model can be developed, accounting for microstructural variations based on thermodynamic and kinetic simulations that predict solute atom concentration, precipitate size, and volume fraction. This approach enables simplified application without the need for repetitive inverse recalibrations, which are common in phenomenological models for flow stress calculations. Additionally, it excludes further parameters, such as tool conditions, that typically influence inverse calibration and limit model performance. This capability decreases the need for costly experimental procedures to determine flow stress properties specific to the heat treatment. The model's performance was validated through investigations on two different material conditions.

(3) The 2D and 3D simulation results demonstrate that an experimentally calibrated Coulomb friction model with a constant apparent friction coefficient friction model possesses sufficient predictive fidelity to resolve the complex tribological contact at the tool–chip interface when approximated by Coulomb sliding friction, also in comparison to a more complex friction model with pressure dependence. According to the presented findings, this observation is specifically valid within the kinematic regime characteristic of drilling where the sliding velocity generally lies within a narrow range as compared to the other machining processes.

(4) The initial examination of the model's performance was performed in the framework of 2D simulations representing the orthogonal cutting with a cutting speed of $v_c = 30$ m/min. The results underscore the potential of the physics-based models by means of reducing the error in calculated contact length $l_{c,sim}$ from $\Delta_{exp,JC16} = -44.6\%$ for the Johnson-Cook reference to $\Delta_{exp,PB9} = -28.9\%$ for the physics-based flow stress model representing a grain size of $d = 9$ µm. This finding was related to the enhanced capability of the models to consider the microstructure in respect of the particular heat treatment when calculating the deformation behaviour in the primary shear zone. In conclusion, a miscalculation of the cutting force with $\Delta_{exp,JC16} = -4.4\%$ for the reference simulation to $\Delta_{exp,PB9} = 5.5\%$ for the physics-based model with a grain size of $d = 9$ µm was stated.

(5) In terms of the predictive accuracy of drilling torque and chip morphology, the physics-based model showed an improvement over the Johnson-Cook model that had already proven to be powerful and also showed good performance in this study. For MC1 a minimum deviation of $\Delta M_{z,PB,33} = -1.86\%$ can be stated and additionally, for MC3 $\Delta M_{z,PB,9} = -0.88\%$, which is a considerable improvement to the already good result of $\Delta M_{z,JC,16} = 5.38\%$ when using the Johnson-Cook flow stress model.

(6) The present study on physics-based constitutive models highlights potential improvements in simulating chip formation during machining. This model allows for reliable predictions of chip formation characteristics under varying cutting parameters and material heat treatment states.

CRediT authorship contribution statement

Jannis Saelzer: Writing – review & editing, Writing – original draft, Visualization. **Amir Malakizadi:** Writing – review & editing, Writing – original draft, Visualization, Validation, Software, Methodology, Investigation, Formal analysis, Data curation, Conceptualization. **Tobias Cyra-Wolf:** Writing – review & editing, Writing – original draft, Visualization, Validation, Software, Methodology, Investigation, Formal analysis, Data curation, Conceptualization. **Dirk Biermann:** Writing – review & editing, Supervision, Project administration, Funding acquisition, Conceptualization. **Youssef Alammari:** Writing – review & editing, Writing – original draft, Visualization.

Declaration of Competing Interest

The authors declare that they have no known competing financial interests or personal relationships that could have appeared to influence the work reported in this paper.

Acknowledgements

Tobias Cyra-Wolf and Dirk Biermann would like to acknowledge the funding of the German Research Foundation (DFG) since the presented work was achieved within the framework of the DFG-project "Simulation and optimization of the coolant flow to reduce the thermal load during discontinuous drilling of Inconel 718" (DFG-Project number: 439920593).

Amir Malakizadi would like to acknowledge the financial supports received from Vinnova (Sweden's Innovation Agency) under the Eureka Smart programme (BRAVE project: 2023–02528) and the Chalmers Centre for Metal Cutting Research (MCR).

Appendix

The recorded compression wave resulting from the pulse that was initiated by the pneumatic pulse generator further expands into the contact area of the specimen with the incident bar, where it is partly reflected and partly transmitted to the contact area with the transmission bar, respectively. Here again, the wave is partly reflected and partly transmitted. The development of the wave motion is recorded by strain gauges attached centrically on the bars. These motions can be related to the stresses, strains, and strain rates occurring during the deformation of the specimen. As the duration of the induced pulse is known, the velocities w_1 and w_2 of the wave at the contact areas can be derived from the elastic strain measured at the bars. Consequently, the strain rate is calculated by considering the length of the specimen l_s:

$$\dot{\varphi}_S = \frac{w_2 - w_1}{l_s}$$

To calculate the stress in the specimen, the forces F_1 and F_2 appearing at the contact areas are related to the cross-section A_s of the specimen in contact with both the bars:

$$\sigma_S = \frac{F_1 + F_2}{2A_s}$$

The described equations can be further developed by assuming that F_1 and F_2 are equal; the elastic strain of the bars is deduced from the equation:

$$w = -c_s\varepsilon$$

In the following, the measured data is transferred to the demanded parameters to describe the deformation behaviour:

$$\sigma_S = \frac{A_B E_B}{A_s}\varepsilon_t$$

$$\dot{\varphi}_s = \frac{2c_s}{l_s}\ \varepsilon_r$$

$$\varphi_S = \frac{2c_s}{l_s}\ \int_0^t \varepsilon_r dt$$

References

[1] Ulutan, D., Ozel, T., 2011. Machining induced surface integrity in titanium and nickel alloys: A review. Int. J. Mach. Tools Manuf. 51, 250–280.
[2] Polvorosa, R., Suárez, A., López de Lacalle, L.N., Cerrillo, I., Wretland, A., Veiga, F., 2017. Tool wear on nickel alloys with different coolant pressures: Comparison of Alloy 718 and Waspaloy. J. Manuf. Process. 26, 44–56.
[3] Xu, D., Liao, Z., Axinte, D., Hardy, M., 2020. A novel method to continuously map the surface integrity and cutting mechanism transition in various cutting conditions. Int. J. Mach. Tools Manuf. 151, 103529.
[4] Liao, Z., Axinte, D., Mieszala, M., M'Saoubi, R., Michler, J., Hardy, M., 2018. On The influence of gamma prime upon machining of advanced nickel based superalloy. CIRP Ann. - Manuf. Technol. 67, 109–112.
[5] Liao, Z., Xu, D., Luna, G.García, Axinte, D., Augustinavicius, G., Sarasua, J.A., Wretland, A., 2021. Influence of surface integrity induced by multiple machining processes upon the fatigue performance of a nickel based superalloy. J. Mater. Process. Tech. 298, 117313.
[6] Olovsjö, S., Wretland, A., Sjöberg, G., 2010. The effect of grain size and hardness of wrought Alloy 718 on the wear of cemented carbide tools. Wear 268, 1045–1052.
[7] Cedergren, S., Olovsjö, S., Sjöberg, G., Nyborg, L., 2013. The effects of grain size and feed rate on notch wear and burr formation in wrought Alloy 718. Int. J. Adv. Manuf. Technol. 67, 1501–1507.
[8] Singh, S.R., Mote, R.G., Mishra, S.K., 2022. The effect of microstructures and precipitates (γ', γ", δ) on machinability of Inconel-718 nickel-based superalloy in turning process. J. Manuf. Process. 82, 374–389.
[9] Liu, Z.F., He, S.M., 2013. Experimental investigation of superfine deep hole drilling mechanism for high temperature alloy 718. Mater. Res. Innov. 17, 229–233.
[10] Pang, K., Wang, D., 2020. Study on the performances of the drilling process of nickel-based superalloy Inconel 718 with differently micro-textured drilling tools. Int. J. Mech. Sci. 180, 105658.
[11] Attanasio, A., Ceretti, E., Outeiro, J., Poulachon, G., 2020. Numerical simulation of tool wear in drilling Inconel 718 under flood and cryogenic cooling conditions. Wear 458-459, 203403.
[12] Jafarian, F., Imaz Ciaran, M., Umbrello, D., Arazola, P.J., Filice, L., Amirabadi, H., 2014. Finite element simulation of machining Inconel 718 alloy including microstructure changes. Int. J. Mech. Sci. 88, 110–121.
[13] Jafarian, F., Umbrello, D., Jabbaripour, B., 2016. Identification of new material model for machining simulation of Inconel 718 alloy and the effect of tool edge geometry on microstructure changes. Simul. Model. Pract. Theory 66, 273–284.
[14] Wedberg, D., Svoboda, A., Lindgren, L.E., 2012. Modelling high strain rate phenomena in metal cutting simulation. Model. Simul. Mater. Sci. Eng. 20, 085006.
[15] Liu, R., Salashoor, M., Melkote, S.N., Marusich, T., 2014. A unified internal state variable material model for inelastic deformation and microstructure evolution in SS304. Mater. Sci. & Eng. A 594, 352–363.
[16] Imbrogno, S., Rinaldi, S., Umbrello, D., Filice, L., Franchi, R., Del Prete, A., 2018. A physically based constitutive model for predicting the surface integrity in machining Waspaloy. Mater. Des. 152, 140–155.
[17] Rinaldi, S., Imbrogno, S., Rotella, G., Umbrello, D., Filice, L., 2019. Physics based modeling of machining Inconel 718 to predict surface integrity modification. Procedia CIRP 82, 350–355.
[18] Chandrasekaran, H., M'Saoubi, R., Chazal, H., 2005. Modelling of material flow stress in chip formation process from orthogonal milling and split Hopkinson bar tests. Mach. Sci. Technol. 9, 131–145.
[19] Zabel, A., Rödder, T., Tiffe, M., 2017. Material Testing and chip formation simulation for different heat treated workpieces of 51CrV4 steel. Procedia CIRP 58, 181–186.
[20] Malakizadi, A., Cedergren, S., Sadik, I., Nyborg, L., 2016. Inverse identification of flow stress in metal cutting process using Response Surface Methodology. Simul. Model. Pract. Theory 60, 40–53.
[21] Afrasiabi, M., Saelzer, J., Berger, S., Iovkov, I., Klippel, H., Röthlin, M., Zabel, A., Biermann, D., Wegener, K., 2021. A Numerical-Experimental Study on Orthogonal Cutting of AISI 1045 Steel and Ti6Al4V Alloy: SPH and FEM Modeling with Newly Identified Friction Coefficients. Metals 11, 1683.
[22] Zhang, N., Klippel, H., Kneubühler, F., Afrasiabi, M., Kuffa, M., Wegener, K., 2024. Investigation of friction modelling on numerical Ti6Al4V cutting simulations. Int. J. Mech. Sci. 274, 109231.
[23] Puls, H., Klocke, F., Lung, D., 2014. Experimental investigation on friction under metal cutting conditions. Wear 310, 63–71.
[24] Saelzer, J., Berger, S., Iovkov, I., Zabel, A., Biermann, D., 2021. Modelling of the friction in the chip formation zone depending on the rake face topography. Wear 477, 203802.
[25] Chaturvedi, M.C., Han, Y.-f, 1983. "Strengthening mechanisms in Inconel 718 superalloy, 1983/03/01 Met. Sci. 17 (3), 145–149. https://doi.org/10.1179/030634583790421032.
[26] Oblak, J.M., Paulonis, D.F., Duvall, D.S., 1974. "Coherency strengthening in Ni base alloys hardened by DO22 γ′ precipitates, 1974/01/01 Metall. Trans. 5 (1), 143–153. https://doi.org/10.1007/BF02642938.
[27] Han, Y.-f, Deb, P., Chaturvedi, M.C., 1982. "Coarsening behaviour of γ″- and γ′-particles in Inconel alloy 718. Met. Sci. 16A (12), 555–562. https://doi.org/10.1179/030634582790427118.
[28] Balan, A., Perez, M., Chaise, T., Cazottes, S., Bardel, D., Corpase, F., Pichot, F., Deschamps, A., De Geuser, F., Nelias, D., 2021. Precipitation of γ″ in Inconel 718 alloy from microstructure to mechanical properties. Materialia 20, 101187.

[29] Toda-Caraballo, I., Rivera-Díaz-del-Castillo, P.E.J., 2015. "Modelling solid solution hardening in high entropy alloys, 2015/02/15/ Acta Mater. 85, 14–23. https://doi.org/10.1016/j.actamat.2014.11.014.
[30] Gypen, L.A., Deruyttere, A., 1977. "Multi-component solid solution hardening, 1977/05/01 J. Mater. Sci. 12 (5), 1028–1033. https://doi.org/10.1007/BF00540987.
[31] Ardell, A.J., 1985. "Precipitation hardening, 1985/12/01 Metall. Trans. A 16 (12), 2131–2165. https://doi.org/10.1007/BF02670416.
[32] Jou, H.-J., Voorhees, P., Olson, G.B., 2004. "Computer simulations for the prediction of microstructure/property variation in aeroturbine disks. Superalloys 2004, 877–886.
[33] Ågren, J., Chen, Q., 2022. "Simplified Growth Model for Multicomponent Systems - Inclusion of PARA and NPLE Conditions, 2022/12/01 J. Phase Equilibria Diffus. 43 (6), 738–744. https://doi.org/10.1007/s11669-022-00969-2.
[34] Wu, K., Chen, Q., Mason, P., 2018. "Simulation of Precipitation Kinetics with Non-Spherical Particles, 2018/10/01 J. Phase Equilibria Diffus. 39 (5), 571–583. https://doi.org/10.1007/s11669-018-0644-1.
[35] Yu, T., Barkar, T., Lancelot, C.-M., Mason, P., 2023. "An ICME Framework to Predict the Microstructure and Yield Strength of INCONEL 718 for Different Heat Treatments. TMS Annual Meeting Exhibition. Springer, pp. 415–427.
[36] Zhang, F., Cao, W., Zhang, C., Chen, S., Zhu, J., Lv, D., 2018. "Simulation of Co-precipitation Kinetics of γ′ and γ″ in Superalloy 718, 2018. In: Cham, E. (Ed.), Proceedings of the 9th International Symposium on Superalloy 718 & Derivatives: Energy, Aerospace, and Industrial Applications. Springer International Publishing, pp. 147–161, 2018.
[37] Ahmadi, M.R., et al., 2017. "Modeling of precipitation strengthening in Inconel 718 including non-sphericalγ″ precipitates", 2017/05/16 Model. Simul. Mater. Sci. Eng. 25 (5), 055005. https://doi.org/10.1088/1361-651x/aa6f54.
[38] Whelan, M.J., 1969. "On the Kinetics of Precipitate Dissolution, 1969/01/01 Met. Sci. J. 3 (1), 95–97. https://doi.org/10.1179/msc.1969.3.1.95.
[39] Semiatin, S.L., et al., 2021. "The Application of Differential Scanning Calorimetry to Investigate Precipitation Behavior in Nickel-Base Superalloys Under Continuous Cooling and Heating Conditions, 2021/09/01 Metall. Mater. Trans. A 52 (9), 3706–3726. https://doi.org/10.1007/s11661-021-06362-x.
[40] Bor, H.Y., Wei, C.N., Nguyen, H.T., Yeh, A.C., Kuo, C.M., 2010. Aging Effects on the γ′ and γ″ Precipitates of Inconel 718 Superalloy. Superalloy 718 Deriv. 678–688. https://doi.org/10.1002/9781118495223.ch52.
[41] Cormier, J., Gadaud, P., Czaplicki, M., Zhang, R.Y., Dong, H.B., Smith, T.M., Zhang, F., Tiley, J.S., Semiatin, S.L., 2021. In-Situ Determination of Precipitation Kinetics During Heat Treatment of Superalloy 718. Metall. Mater. Trans. Metall. Mater. Trans. A 52, 501–511.
[42] Volpato, G.M., Vollhüter, J., Diepold, B., Meier, M.S., Pröbstle, M., Göken, M., Niendorf, T., Felfer, P., Neumeier, S., 2025. Revealing the γ′ and γ″ Phase Fractions of Additively Manufactured and Differently Heat-Treated Nickel-Base Superalloy IN718 by Atom Probe Tomography and Their Impact on Mechanical Properties. Adv. Eng. Mater. 27 (9), 2401954.
[43] Malmelöv, A., Fisk, M., Lundbäck, A., Lindgren, L.-E., 2020. "Mechanism Based Flow Stress Model for Alloy 625 and Alloy 718. Materials 13 (24), 5620.
[44] Fisk, M., Ion, J.C., Lindgren, L.-E., 2014. "Flow stress model for IN718 accounting for evolution of strengthening precipitates during thermal treatment. Comput. Mater. Sci. 82, 531–539.
[45] Zaiser, M., Seeger, A., 2002. "Chapter 56 Long-range internal stresses, dislocation patterning and work-hardening in crystal plasticity. In: Nabarro, F.R.N., Duesbery, M.S. (Eds.), Dislocations in Solids, 11. Elsevier, pp. 1–100.
[46] Kuhlmann-Wilsdorf, D., 1985. "Theory of workhardening 1934-1984, 1985/12/01 Metall. Trans. A 16 (12), 2091–2108. https://doi.org/10.1007/BF02670414.
[47] Lavrentev, F.F., 1980. "The type of dislocation interaction as the factor determining work hardening, 1980/12/01/ Mater. Sci. Eng. 46 (2), 191–208. https://doi.org/10.1016/0025-5416(80)90175-5.
[48] Argon, A., 2007. OUP. Strengthening Mechanisms in Crystal Plasticity. Oxford.
[49] Peierls, R., 1940. "The size of a dislocation. Proc. Phys. Soc. 52 (1), 34.
[50] Nabarro, F.R.N., 1947. "Dislocations in a simple cubic lattice, 1947/03/01 Proc. Phys. Soc. 59 (2), 256. https://doi.org/10.1088/0959-5309/59/2/309.
[51] Joós, B., Duesbery, M.S., 1997. "The peierls stress of dislocations: an analytic formula, 01/13/ Phys. Rev. Lett. 78 (2), 266–269. https://doi.org/10.1103/PhysRevLett.78.266.
[52] Frost, H.J., Ashby, M.F., 1982. Deformation-mechanism maps: the plasticity and creep of metals and ceramics. Pergamon press.
[53] Orowan, E., 1940. "Problems of plastic gliding, 1940/01/01 Proc. Phys. Soc. 52 (1), 8. https://doi.org/10.1088/0959-5309/52/1/303.
[54] Kocks, U.F., As, A., Mf, A., 1975. "Thermodynamics and kinetics of slip, 1975.
[55] Labusch, R., 1970. "A Statistical Theory of Solid Solution Hardening. Phys. Status Solidi (b) 41 (2), 659–669. https://doi.org/10.1002/pssb.19700410221.
[56] Lubarda, V.A., 2003. "On the effective lattice parameter of binary alloys, 2003/01/01/ Mech. Mater. 35 (1), 53–68. https://doi.org/10.1016/S0167-6636(02)00196-5.
[57] Ahmadi, M.R., et al., 2022. "Coherency strengthening of oblate precipitates extended in the {100} plane of fcc crystals: Modeling and experimental validation, 2022/03/01/ Materialia 21, 101328. https://doi.org/10.1016/j.mtla.2022.101328.
[58] Gerold, V., Haberkorn, H., 1966. On the Critical Resolved Shear Stress of Solid Solutions Containing Coherent Precipitates. Phys. Status Solidi (b) 16 (2), 675–684. https://doi.org/10.1002/pssb.19660160234.
[59] Taylor, G.I., 1934. The mechanism of plastic deformation of crystals. Part I.—Theoretical. Proc. R. Soc. Lond. Ser. A Contain. Pap. A Math. Phys. Character 145 (855), 362–387.
[60] Kocks, U.F., Mecking, H., 2003. Physics and phenomenology of strain hardening: the FCC case, 2003/01/01/ Prog. Mater. Sci. 48 (3), 171–273. https://doi.org/10.1016/S0079-6425(02)00003-8.
[61] Gladman, T., 1999. Precipitation hardening in metals, 1999/01/01 Mater. Sci. Technol. 15 (1), 30–36. https://doi.org/10.1179/026708399773002782.
[62] Nabarro, F.R.N., 1989. Work hardening and dynamical recovery of F.C.C. metals in multiple glide, 1989/06/01/ Acta Metall. 37 (6), 1521–1546. https://doi.org/10.1016/0001-6160(89)90122-3.
[63] Simo, J.C., Taylor, R.L., 1986. A return mapping algorithm for plane stress elastoplasticity. Int. J. Numer. Methods Eng. 22 (3), 649–670. https://doi.org/10.1002/nme.1620220310.
[64] Moretti, M.A., Lindgren, L.E., Åkerström, P., 2023. Physics-based flow stress model for alloy 718. Metall. Mater. Trans. A 54 (5), 1985–1997.
[65] ⟨https://www.specialmetals.com/documents/technical-bulletins/inconel/inconel-alloy-718.pdf⟩.
[66] Iturbe, A., Giraud, E., Hormaetxe, E., Garay, A., Germain, G., Ostolaza, K., Arrazola, P.J., 2017. Mechanical characterization and modelling of Inconel 718 material behavior for machining process assessment. Materials Science Engineering A 682, 441–453.
[67] Malakizadi, A., Oberbeck, J.N., Magnevall, M., Krajnik, P., 2019. A new constitutive model for cutting simulation of 316L austenitic stainless steel. Procedia CIRP 82, 53–58.
[68] Shi, B., Attia, H., Tounsi, N., 2010. Identification of Material Constitutive Laws for Machining – Part II: Generation of the Constitutive Data and Validation of the Constitutive Law. J. Manuf. Sci. Eng. 132 (5), 051009.
[69] Bonnet, C., Valiorgue, F., Rech, J., Claudin, C., Hamdi, H., Bergheau, J.M., Gilles, P., 2008. Identification of a friction model – Application to the context of dry cutting of an AISI 316L austenitic stainless steel with a TiN coated carbide tool. Int. J. Mach. Tools Manuf. 48, 1211–1223.
[70] Melkote, S.N., Grzesik, W., Outeiro, J., Rech, J., Schulze, V., Attia, H., Arrazola, P. J., M'Saoubi, R., Saldana, C., 2017. Advances in material and friction data for modelling of metal machining. CIRP Ann. 66, 731–754.